

CORRELATIONAL LAGRANGIAN SCHRÖDINGER BRIDGE: LEARNING DYNAMICS WITH POPULATION-LEVEL REGULARIZATION

Anonymous authors

Paper under double-blind review

ABSTRACT

Modeling population dynamics is a fundamental problem with broad scientific applications. Motivated by real-world applications including biosystems with diverse populations, we consider a class of population dynamics modeling with two technical challenges: (i) dynamics to learn for individual particles are *heterogeneous* and (ii) available data to learn from are not *time-series* (i.e, each individual’s state trajectory over time) but *cross-sectional* (i.e, the whole population’s aggregated states without individuals matched over time). To address the challenges, we introduce a novel computational framework dubbed **correlational Lagrangian Schrödinger bridge (CLSB)** that builds on optimal transport to “bridge” cross-sectional data distributions. In contrast to prior methods regularizing all individuals’ transport “costs” and then applying them to the population *homogeneously*, CLSB directly regularizes *population* cost allowing for population *heterogeneity* and potentially improving model generalizability. Specifically our contributions include **(1)** a novel population perspective of the transport cost and a new class of population regularizers capturing the temporal variations in multivariate relations, with the tractable formulation derived, **(2)** three domain-informed instantiations of population regularizers on covariance, and **(3)** integration of population regularizers into data-driven generative models as constrained optimization and an approximate numerical solution, with further extension to conditional generative models. Empirically, we demonstrate the superiority of CLSB in single-cell sequencing data analyses (including cell differentiation and drug-conditioned cell responses) and opinion depolarization. Codes will be released upon acceptance.

1 INTRODUCTION

Population dynamics sheds insight on the temporal evolution of systems, such as cytodynamics (La Manno et al., 2018), fluid mechanics (Kundu et al., 2015) and single-cell omics (Macosko et al., 2015), yet their direct observation is often restricted. Motivated by such real-world systems, this paper targets generative population-dynamics models for heterogeneous populations whose states are not available to track individual trajectories (time-series data) but only observed at the population level at times (cross-sectional data as referred to in (Tong et al., 2020; Koshizuka & Sato, 2022)). In the cross-sectional setting, states of a population are measured at each timestamp without individual match or even population match across timestamps. In other words, the cross-sectional data are sampled independently at various timestamps rather than jointly across timestamps. One such example is single-cell omics that study cell populations behaviours with unprecedented data (Gaston & Spicer, 2013; Purvis & Hector, 2000): As each measurement at any timestamp is made with cells fixed and stained or chemically destroyed, measurements across time or condition can only be observed from different samples of the cell population but not individual trajectories of the same set of cells (e.g., developmental/immun omics (Keller, 2005; Schluter et al., 2020)).

Lacking individual trajectory data for direct supervision, current machine learning methods attempt to “bridge” among cross-sectional distributions under certain principles, such as optimal transport (Villani et al., 2009; Santambrogio, 2015). To characterize the evolutionary nature of the system, besides matching the cross-sectional distributions, these methods also regularize certain transport costs, which are typically determined by the domain knowledge of the system. These costs are asso-

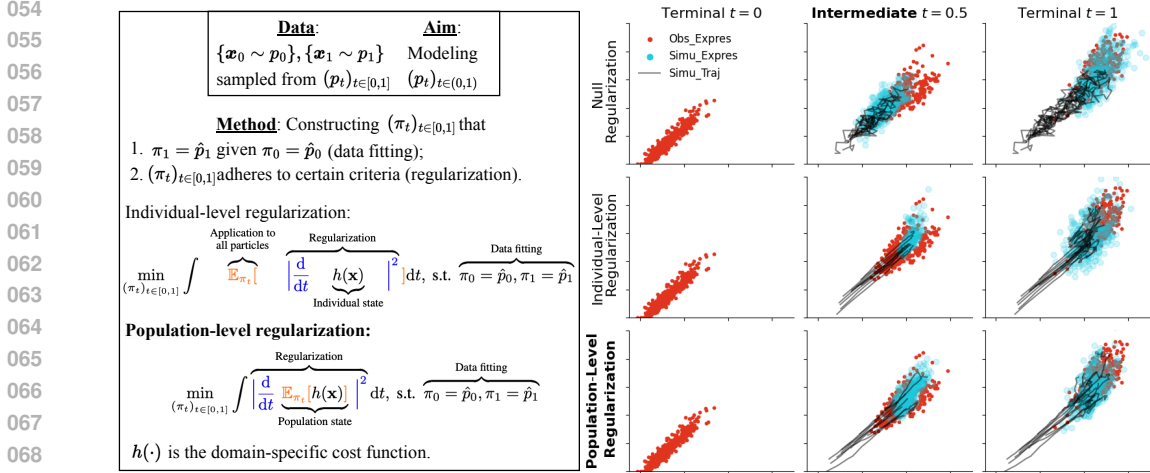


Figure 1: (Left) Overview of the proposed approach and (right) computational simulation of the expressions of gene ABCA3 (x-axis) and A1BG (y-axis) during the embryonic stem cell development under different regularizations. Notably, our proposed population-level regularization facilitates a more accurate modeling of distributions, with quantitative evidence detailed in Sec. 4 and more visualization in Appdx. I.

ciated with certain physical quantities on individual particle’s states, such as the restraint on particle motions (Schiebinger et al., 2019; Yang & Uhler, 2018), or the alignment to empirical densities or velocities (Tong et al., 2020; Koshizuka & Sato, 2022). However, some physical quantities are only defined in the population level. For example of gene co-expressions: Gene expression covariance is only among a population of cells, while each individual cell has different/heterogeneous gene expressions. Uniformly restraining the states of individuals is thus oblivious to such knowledge.

To fill such a gap, we hypothesize that principled regularizers, if directly and appropriately formulated for the states of the population (as opposed to the states of individuals), can lead to more accurate modeling of dynamics for heterogeneous systems. The rationale of the hypothesis is directly related to the needs: As the ensemble statistics of individual states, population states (i) respect the diversity (heterogeneity) of individual states, and importantly, (ii) can accommodate domain priors previously not utilized at the population level, e.g., the co-expression relations among genes of cellular systems, derived from bulk sequencing techniques (Stuart et al., 2003; Horvath & Dong, 2008). A nutshell overview of individual v.s. population restraint can be found in Fig. 1 (left).

Contributions. We propose a novel learning framework dubbed **correlational Lagrangian Schrödinger bridge (CLSB)** to model the dynamics of heterogeneous systems from *cross-sectional data using principled regularization at the population level* (see Fig. 1 for an overview). To the best of our knowledge, CLSB is the *first* framework to incorporate population-level domain prior into diffusion Schrödinger bridge for generative dynamics, with *substantial* benefits demonstrated for heterogeneous systems including biosystems. Specifically we make the following contributions.

(1) A novel perspective of the principled regularizer for transport cost with tractable formulations. *How to formulate the principled regularizer at the population level?* Motivated by the principle of least action (Schiebinger et al., 2019; Yang & Uhler, 2018), we propose to *conserve certain population states* when bridging across cross-sectional data, where the extent of conservation is measured by the temporal variations in certain statistical characteristics. Accordingly, we introduce a new category of population regularizers termed *correlational Lagrangian*, which is designed to capture the extent of temporal changes in multivariate relations expressed as moments (Parzen, 1999; Kumar & Varaiya, 2015) (Sec. 3.1). As the novel population regularizer poses a challenge of intractability that it cannot be computed numerically, we derive a computationally tractable formulation by applying the Fokker-Planck equation (Risken, 1996) with mild assumptions (Sec. 3.2).

(2) Effective domain-informed instantiations of population regularization. *How to instantiate population regularizers with domain-informed priors?* The generic formulation of the correlational Lagrangian is highly versatile, that is able to characterize arbitrary multivariate relations in arbitrary orders. Inspired by the concept of *co-expression stability* in genetics that the co-expression rela-

tions among genes should be robust to environments (Patil et al., 2011; Srihari & Leong, 2012), we propose to enforce temporal conservation on the states of covariance, focusing on the 1st- and 2nd-order variations of bivariate statistics, termed *covariance kinetics* (Sec. 3.3.1). We also leverage the existing evidence of co-expression by constructing *covariance potential*, which enforces alignment between the modeled covariance and the observed interactions from literature (Sec. 3.3.2).

(3) Practical numerical solution to model training. *How to integrate population regularizers with data-driven generative modeling of dynamics?* We formulate a *constrained optimization* problem referred to as CLSB, which is designed to minimize correlational Lagrangian subject to the constraints imposed by cross-sectional observations, optimizing on the parametrized dynamics using neural stochastic differential equations (SDEs) (Li et al., 2020; Tzen & Raginsky, 2019). To solve CLSB, we propose a *numerical approximation* via unconstrained optimization (Sec. 3.4).

Furthermore, we extend the CLSB framework into conditional dynamics generation, by re-engineering neural SDEs for taking the additional conditions as inputs. Empirically, we validate that CLSB outperforms state-of-the-art competitors in the experiments of (unconditional) developmental simulation and (conditional) drug-response prediction in cellular systems (Sec. 4). Population regularizers also showed benefits in opinion depolarization (Appdx. I).

2 PRELIMINARIES

Data generation from dynamics.

The main notation used in the paper is described in Tab. 1. Let’s assume that data are generated from a stochastic process $(\mathbf{x}_t)_{t \in [0,1]}$ following the distribution $(p_t)_{t \in [0,1]}$ and obeying the dynamics below:

$$d\mathbf{x}_t = \mathbf{f}_t(\mathbf{x}_t)dt + \mathbf{G}_t(\mathbf{x}_t)d\mathbf{w}_t, \quad (1)$$

where $\mathbf{x}_t \in \mathbb{R}^d$, $\mathbf{f}_t : \mathbb{R}^d \rightarrow \mathbb{R}^d$ is the drift function, $(\mathbf{w}_t)_{t \in [0,1]}$ is a Wiener process in $\mathbb{R}^{d_{\text{wic}}}$, and $\mathbf{G}_t : \mathbb{R}^d \rightarrow \mathbb{R}^{d \times d_{\text{wic}}}$ is the diffusion function. Consequently, the evolution of marginal distribution p_t satisfies the Fokker–Planck equation (Risken, 1996) as:

$$\frac{\partial}{\partial t} p_t(\mathbf{x}) = -\nabla \cdot (p_t(\mathbf{x}) \mathbf{f}_t(\mathbf{x})) + \frac{1}{2} (\nabla \nabla^\top) \cdot (p_t(\mathbf{x}) \mathbf{G}_t(\mathbf{x}) \mathbf{G}_t^\top(\mathbf{x})). \quad (2)$$

Generative modeling via Schrödinger bridge. As stated in Eq. (2), the distribution $(p_t)_{t \in [0,1]}$ is characterized by the drift and diffusion terms in Eq. (1). Thus, by parametrizing $\mathbf{f}_t(\cdot)$ and $\mathbf{G}_t(\cdot)$ with neural networks $\mathbf{v}_t(\cdot; \theta)$ and $\Sigma_t(\cdot; \theta)$, respectively, and with the observations from the finite-dimensional distribution as $\mathcal{D}_{\text{fdim}} = \{\mathbf{x}_t^{(i)} : t \in \{t_1, \dots, t_s\}, i \in \{1, \dots, n\}, (\mathbf{x}_{t_1}^{(i)}, \dots, \mathbf{x}_{t_s}^{(i)}) \sim p_{t_1, \dots, t_s}\}$ where $t_1 = 0, t_s = 1$, a line of prior works attempt to construct the generative model $(\pi_t)_{t \in [0,1]}$ (parametrized by $\mathbf{v}_t(\cdot; \theta), \Sigma_t(\cdot; \theta)$) via solving the collective form of the (static) Schrödinger bridge problem as (De Bortoli et al., 2021; Liu et al., 2022):

$$\min_{\theta} \frac{1}{s-1} \sum_{i=1}^{s-1} \text{KL}(\pi_{t_i, t_{i+1}} \| \hat{p}_{t_i, t_{i+1}}), \quad (\text{Trajectory Fitting}) \quad (3.1)$$

$$\text{s.t. } \pi_{t_i} = \hat{p}_{t_i}, i \in \{1, \dots, s\}, \quad (\text{Marginal Fitting}) \quad (3.2)$$

$$(\pi_t)_{t \in [0,1]} \text{ is induced from } \mathbf{v}_t(\cdot; \theta), \Sigma_t(\cdot; \theta), t \in [0, 1] \text{ via Eq. (1), } (\text{Parametrization}) \quad (3.3)$$

where $\hat{p}_{t_1, \dots, t_s}$ is the empirical distribution of $\mathcal{D}_{\text{fdim}}$. Conceptually, Optimization in (3) requires the parametrized $(\pi_t)_{t \in [0,1]}$ to align with the reference joint distribution $\hat{p}_{t_i, t_{i+1}}$ as well as marginal \hat{p}_{t_i} of the data.

Lagrangian Schrödinger bridge for cross-sectional data. Trajectory observations $\mathcal{D}_{\text{fdim}}$ from the finite-dimensional distribution are not always available. In practice, data might be only observed

Table 1: Notation settings.

Notations	Descriptions
Upright letters (\mathbf{x}) Italicized letters (\mathbf{x})	Random variables Their realizations
Lowercase boldfaced (\mathbf{x}) Uppercase boldfaced (\mathbf{X}) Lowercase non-boldfaced (x)	Vectors Matrices Scalars
Superscripts with brackets ($\mathbf{x}^{(i)}$) Subscripts with square brackets ($\mathbf{x}_{[i]}$)	For multiple realizations For indexed elements
∇ \cdot	Divergence operator Inner product
s d m, k	Number of Time Stamps Variable Dimensionality Order of Prior (in Derivative)
$\tilde{\mathcal{M}}$ \mathcal{M}	Multiset of Variable Indices Set Collection of Multisets $\tilde{\mathcal{M}}$

from the marginal distributions $\mathcal{D}_{\text{marg}} = \{\mathbf{x}_t^{(i)} : t \in \{t_1, \dots, t_s\}, i \in \{1, \dots, n\}, \mathbf{x}_t^{(i)} \sim p_t\}$ where s is the number of time stamps which can be observed. For such cross-sectional observations, Opt. (3) is not applicable since the reference distributions $\hat{p}_{t_i, t_{i+1}}, i \in \{1, \dots, s-1\}$ in the objective (3.1) are not available. Accordingly, existing solutions propose to solve an alternative optimization problem called Lagrangian Schrödinger bridge (LSB), which adopts the *principled regularizer of least action* instead to guide the evolution of dynamics as (Koshizuka & Sato, 2022; Neklyudov et al., 2023):

$$\min_{\theta} \frac{1}{(s-1)d} \sum_{i=1}^{s-1} \sum_{j=1}^d \int_{t_i}^{t_{i+1}} L_{\text{ind}}(\pi_t, j, m) dt, \quad \text{s.t. Constraints (3.2) \& (3.3),} \quad (4)$$

where $L_{\text{ind}}(\pi_t, j, m) = \underbrace{\mathbb{E}_{\pi_t}}_{\text{Summarization}} \left[\underbrace{\left| \frac{d}{dt} ((\mathbf{x}_{t,[j]})^m) \right|^2}_{\text{Lagrangian to measure individual action}} \right], \quad (\text{Principled Regularizer for Individuals})$

where $\hat{p}_{t_1, \dots, t_s}$ is overwrote **re-wrote** as the empirical distribution of $\mathcal{D}_{\text{marg}}$. It is typical to set $m = 1$ and approximate the Lagrangian with expectation as $|\frac{d}{dt} \mathbf{x}_{t,[j]}|^2 \approx |v_{t,[j]}(\mathbf{x}_t; \theta)|^2 + \Sigma_{t,[j,:]}^{\top}(\mathbf{x}_t; \theta) \Sigma_{t,[j,:]}(\mathbf{x}_t; \theta)$ to restrain individual motions (Mikami, 2008; Tong et al., 2020). More related works are detailed in Appdx. C.

3 METHODS

We first introduce a novel regularizer from a fresh perspective of population state conservation (Sec. 3.1) and then address the intractability issue of regularizers resulting from the implicit distribution parametrization in diffusion models, by using the Fokker-Planck equation (Sec. 3.2). For practical implementation, we provide three biology-inspired instantiations of covariance regularizers (Sec. 3.3.1) and an approximate numerical solution to unconstrained optimization of the framework, while the exact solution of constrained, non-convex optimization is daunting (Sec. 3.4).

3.1 THE PRINCIPLE OF LEAST POPULATION ACTION

The Lagrangian Schrödinger bridge (LSB) problem (4) enforces the least actions for individual particles during the evolution, i.e., the conservation of individual states. Two assumptions could be violated in real-world applications such as single-cell omics. First, time-series data for individuals may not be available, e.g., measuring trajectories of individual cells is still technically challenging. Second, particles could be heterogeneous in nature (Gaston & Spicer, 2013; Purvis & Hector, 2000), while the simple regularizer $L_{\text{ind}}(\cdot)$ is formulated for individual states (via action measurement $|\frac{d}{dt}(\cdot)|^2$) and then applied homogeneously to all particles (via summarization $\mathbb{E}_{\pi_t}[\cdot]$), which violates the nature of population heterogeneity.

To address the two challenges above, we propose to shift the focus of regularizers to population-level and reorient the emphasis of conservation strategies to population states. Specifically, we formulate an optimization problem with population regularizer $L_{\text{pop}}(\cdot)$, by interchanging the order of action measurement $|\frac{d}{dt}(\cdot)|^2$ and summarization $\mathbb{E}_{\pi_t}[\cdot]$ in $L_{\text{ind}}(\cdot)$ as follows:

$$\min_{\theta} \frac{1}{(s-1)d} \sum_{i=1}^{s-1} \sum_{j=1}^d \int_{t_i}^{t_{i+1}} L_{\text{pop}}(\pi_t, j, m) dt, \quad \text{s.t. Constraints (3.2) \& (3.3),} \quad (5)$$

where $L_{\text{pop}}(\pi_t, j, m) = \underbrace{\left| \frac{d}{dt} \mathbb{E}_{\pi_t} [(\mathbf{x}_{t,[j]})^m] \right|^2}_{\text{Action measurement}}, \quad (\text{Principled Regularizer for Population})$

where it is assumed $\int |\mathbf{x}_{[j]}|^m \pi_t(\mathbf{x}) d\mathbf{x} < \infty, j \in \{1, \dots, d\}$ (Spanos, 2019) for the interchangeability. The proposed population-level regularizer $L_{\text{pop}}(\cdot)$ essentially captures the temporal variations in certain population characteristics, contrasting with the focus on individual-state dynamics in $L_{\text{ind}}(\cdot)$. In this context, the population state is quantified by the m th-order moment of each variable j , the determinacy of which is studied in the Hamburger moment problem (Shohat & Tamarkin, 1950; Akhiezer, 2020). Thus, Opt. (5) aims to find the evolution $(\pi_t)_{t \in [t_i, t_{i+1}]}$ between terminal distributions $\pi_{t_i} = \hat{p}_{t_i}$ and $\pi_{t_{i+1}} = \hat{p}_{t_{i+1}}$ such that the characteristics of distributions evolve smoothly.

Moving beyond Opt. (5) we will present a conceptually more complete and computationally tractable formulation for population regularizers in the next subsections.

3.2 CORRELATIONAL LAGRANGIAN SCHRÖDINGER BRIDGE

Conservation of correlation during evolution. The initial extension from individual to population regularization in Opt. (5) falls short in capturing the relations among data variables, which accounts for a rich family of observed behaviors especially in biological systems (Patil et al., 2011; Srihari & Leong, 2012). Thus, we propose to extend the objective formulation in Opt. (5) by involving multivariate relations, resulting in the optimization problem referred as correlational Lagrangian Schrödinger bridge (CLSB) as:

$$\min_{\theta} \frac{1}{(s-1)|\mathcal{M}|} \sum_{i=1}^{s-1} \sum_{\tilde{\mathcal{M}} \in \mathcal{M}} \int_{t_i}^{t_{i+1}} L_{\text{corr}}(\pi_t, \tilde{\mathcal{M}}, k) dt, \quad \text{s.t. Constraints (3.2) \& (3.3)} \quad (6)$$

$$\text{where } L_{\text{corr}}(\pi_t, \tilde{\mathcal{M}}, k) = \underbrace{\left| \frac{d^k}{dt^k} \mathbb{E}_{\pi_t} \left[\underbrace{\prod_{(j,m) \in \tilde{\mathcal{M}}} (x_{t,[j]})^m}_{\text{Correlational Lagrangian}} \right] \right|^2}_{\text{Correlational Lagrangian}} \quad \text{(Population Regularizer on Multivariate Correlation)}$$

where $k \in \mathbb{Z}_{>}$, $\mathcal{M} = \{\dots, \tilde{\mathcal{M}}_i, \dots\}$ that each $\tilde{\mathcal{M}}_i = \{(j, \tilde{m}_i(j)) : j \in \tilde{\mathcal{M}}_i \subset \{1, \dots, d\}, \tilde{m}_i : \{1, \dots, d\} \rightarrow \mathbb{Z}_{>}\}$ is a multiset consisting of variable indices and their corresponding occurrences, identifying the targeted multivariate relation which is quantified by the mixed moment (Parzen, 1999; Kumar & Varaiya, 2015). We refer to $L_{\text{corr}}(\cdot)$ as *correlational Lagrangian* capturing temporal variations in multivariate correlations.

The CLSB formulation (6) is the more general framework, capable of imposing domain priors for arbitrary multivariate relations (specified by $\tilde{\mathcal{M}}$ in $L_{\text{corr}}(\cdot)$) in arbitrary order (specified by k). For instance, by setting $k = 1$ and $\mathcal{M} = \{\tilde{\mathcal{M}}_j : \tilde{\mathcal{M}}_j = \{(j, m)\}, j = 1, \dots, d\}$, CLSB degenerates to Opt. (5) that involves null multivariate correlations.

Analytical expression of correlational Lagrangian. The current formulation of correlational Lagrangian $L_{\text{corr}}(\cdot)$ in Opt. (6) is not yet in a tractable form for practical implementation due to the existence of the k -order time derivative. Our following proposition provides the derivation of tractable analytical expressions under mild assumptions.

Proposition 1. For $k = 1$, correlational Lagrangian in Opt. (6) admits the analytical expression as:

$$L_{\text{corr}}(\pi_t, \tilde{\mathcal{M}}, 1) = \left| \mathbb{E}_{\pi_t} \left[\nabla \left(\prod_{(j,m) \in \tilde{\mathcal{M}}} (x_{t,[j]})^m \right) \cdot \underbrace{\mathbf{v}_t(\mathbf{x}_t; \theta)}_{\text{Variation resulting from drift } \mathbf{v}_t(\cdot; \theta)} \right] \right| + \frac{1}{2} \mathbb{E}_{\pi_t} \left[\left(\nabla \nabla^\top \left(\prod_{(j,m) \in \tilde{\mathcal{M}}} (x_{t,[j]})^m \right) \right) \cdot \underbrace{(\boldsymbol{\Sigma}_t(\mathbf{x}_t; \theta) \boldsymbol{\Sigma}_t^\top(\mathbf{x}_t; \theta))}_{\text{Variation resulting from diffusion } \boldsymbol{\Sigma}_t(\cdot; \theta)} \right) \right]^2, \quad (7)$$

if for the set of functions $\mathcal{H} = \{h(\mathbf{x})\pi_t(\mathbf{x})\mathbf{v}_t(\mathbf{x}), \pi_t(\mathbf{x})\mathbf{D}(\mathbf{x})\nabla h(\mathbf{x}), \pi_t(\mathbf{x})\nabla^\top \mathbf{D}_t(\mathbf{x})h(\mathbf{x}), h(\mathbf{x})\mathbf{D}_t(\mathbf{x})\nabla \pi_t(\mathbf{x})\}$ (θ is omitted for simplicity) that $h(\mathbf{x}) = \prod_{(j,m) \in \tilde{\mathcal{M}}} (x_{t,[j]})^m$, $\mathbf{D}_t(\mathbf{x}) = \boldsymbol{\Sigma}_t(\mathbf{x})\boldsymbol{\Sigma}_t^\top(\mathbf{x})$, it satisfies: (i) Continuity: $h' \in \mathcal{H}$ is continuously differentiable w.r.t. \mathbf{x} ; (ii) Light tail: The probability density function $\pi_t(\mathbf{x})$ is characterized by tails that are sufficiently light, such that $\oint_{S_\infty} h'(\mathbf{x}) \cdot d\mathbf{a} = 0$ for $h' \in \mathcal{H}$, where \mathbf{a} is the outward pointing unit normal on the S_∞ boundary.

For $k \geq 2$, correlational Lagrangian $L_{\text{corr}}(\pi_t, \tilde{\mathcal{M}}, k)$ in Opt. (6) admits a more complex analytical expression, which can be derived iteratively in a similar way if certain conditions of continuity and light tails are met. The detailed formulation is postponed to Appdx. A to avoid distraction.

Proof. See Appdx. A.

The key step in the derivation involves applying the Fokker–Planck equation (2) to establish a connection between the temporal variation $\frac{d}{dt} \mathbb{E}_{\pi_t}[\cdot]$ and the (parametrized) force field $\mathbf{v}_t(\cdot; \theta)$, $\boldsymbol{\Sigma}_t(\cdot; \theta)$.

Both conditions are moderate and can be easily ensured by appropriately constructing the architectures of the drift and diffusion functions (Schulz et al., 2018; Song et al., 2020). Thereby, Propos. 1 enables the tractable computation of correlational Lagrangian for practical implementation.

3.3 DOMAIN-INFORMED INSTANTIATIONS OF CORRELATIONAL LAGRANGIAN IN BIOLOGICAL SYSTEMS

3.3.1 COVARIANCE KINETICS

Conserving bivariate relations for co-expression stability. Existing literature in genetics indicates the phenomenon of co-expression stability, i.e., the co-expression among genes could be robust to environments (Patil et al., 2011; Srihari & Leong, 2012). We numerically validate such phenomena in our dataset (see Appdx. D for details). We are therefore inspired to incorporate such prior into the population regularizer, by focusing correlational Lagrangian specifically on bivariate relations, thereby restraining temporal variations of the states of covariance. We term it as *covariance kinetics* to demonstrate the idea of restricting the “motion” of the population (Frost & Pearson, 1961; Lifschitz & Pitajewski, 1983), with two specific instantiations as follows.

Instantiation 1: Restraining the “velocity” of covariance. The first instantiation to enforce models simulate stably co-expressed genes in cells, is through restraining the 1st-order moment of the covariance, such that it (representing co-expression relations) changes slowly during temporal evolution. In formulation, denoting $\mathcal{M}_{\text{cov}} = \left\{ \{(i, 1), (j, 1)\} : i \in \{1, \dots, d\}, j \in \{1, \dots, d\} \right\}$ for all the pairs among d variables, the objective in Opt. (6) is analytically instantiated as:

$$\begin{aligned} \sum_{\tilde{\mathcal{M}} \in \mathcal{M}_{\text{cov}}} L_{\text{corr}}(\pi_t, \tilde{\mathcal{M}}, 1) &= \left\| \frac{d}{dt} \mathbb{E}_{\pi_t} [\mathbf{x}_t \mathbf{x}_t^\top] \right\|_{\text{F}}^2 \\ &= \left\| \mathbb{E}_{\pi_t} [\mathbf{x}_t \mathbf{v}_t(\mathbf{x}_t)^\top + \mathbf{v}_t(\mathbf{x}_t) \mathbf{x}_t^\top + \frac{1}{2} \Sigma_t(\mathbf{x}_t) \Sigma_t^\top(\mathbf{x}_t)] \right\|_{\text{F}}^2. \end{aligned} \quad (8)$$

Instantiation 2: Restraining the “acceleration” of covariance. The second instantiation is more relaxed, allowing greater temporal variation in co-expression, which however, should not be “irregular”. We **achieve** this by restraining the second-order moment of the covariance, ensuring that it evolves “regularly” during dynamics, with the objective formulated as:

$$\begin{aligned} \sum_{\tilde{\mathcal{M}} \in \mathcal{M}_{\text{cov}}} L_{\text{corr}}(\pi_t, \tilde{\mathcal{M}}, 2) &= \left\| \frac{d^2}{dt^2} \mathbb{E}_{\pi_t} [\mathbf{x}_t \mathbf{x}_t^\top] \right\|_{\text{F}}^2 \\ &= \left\| \mathbb{E}_{\pi_t} \left[\mathbf{x}_t \left(\frac{d}{dt} \mathbf{v}_t(\mathbf{x}_t) \right)^\top + \left(\frac{d}{dt} \mathbf{v}_t(\mathbf{x}_t) \right) \mathbf{x}_t^\top + \frac{1}{2} \frac{d}{dt} (\Sigma_t(\mathbf{x}_t) \Sigma_t^\top(\mathbf{x}_t)) \right] \right. \\ &\quad + \mathbb{E}_{\pi_t} \left[\mathbf{x}_t (\nabla \mathbf{v}_t(\mathbf{x}_t) \mathbf{v}_t(\mathbf{x}_t))^\top + (\nabla \mathbf{v}_t(\mathbf{x}_t) \mathbf{v}_t(\mathbf{x}_t)) \mathbf{x}_t^\top + 2 \mathbf{v}_t(\mathbf{x}_t) \mathbf{v}_t(\mathbf{x}_t)^\top + \frac{1}{2} \nabla (\Sigma_t(\mathbf{x}_t) \Sigma_t^\top(\mathbf{x}_t))_{i_1 i_2 i_3} \mathbf{v}_t^{i_3}(\mathbf{x}_t) \right] \\ &\quad + \mathbb{E}_{\pi_t} \left[\nabla \mathbf{v}_t(\mathbf{x}_t) \Sigma_t(\mathbf{x}_t) \Sigma_t^\top(\mathbf{x}_t) + \Sigma_t(\mathbf{x}_t) \Sigma_t^\top(\mathbf{x}_t) \nabla^\top \mathbf{v}_t(\mathbf{x}_t) + \frac{1}{2} \mathbf{x}_t (\nabla \nabla^\top (\mathbf{v}_t(\mathbf{x}_t))_{i_1 i_2 i_3} (\Sigma_t(\mathbf{x}_t) \Sigma_t^\top(\mathbf{x}_t))^{i_2 i_3}) \right. \\ &\quad \left. + \frac{1}{2} (\nabla \nabla^\top (\mathbf{v}_t(\mathbf{x}_t))_{i_1 i_2 i_3} (\Sigma_t(\mathbf{x}_t) \Sigma_t^\top(\mathbf{x}_t))^{i_2 i_3}) \mathbf{x}_t^\top + \frac{1}{4} \nabla \nabla^\top (\Sigma_t(\mathbf{x}_t) \Sigma_t^\top(\mathbf{x}_t))_{i_1 i_2 i_3 i_4} (\Sigma_t(\mathbf{x}_t) \Sigma_t^\top(\mathbf{x}_t))^{i_3 i_4} \right] \left. \right\|_{\text{F}}^2, \end{aligned} \quad (9)$$

where we adopt the Einstein notation $C = A_{ij} B^{jk}$ (Barr, 1991) for tensor operations that $C_{[i,k]} = \sum_j A_{[i,j]} B_{[j,k]}$. The matrix-form derivations of instantiations (8) & (9) are based on Propos. 1, and we provide a more detailed explanation of the derivation of complicated Eq. (9) in Appdx. B.

Standardized covariance kinetics within a projected space. The original covariance may be sensitive to dataset-dependent parameters, such as batch effects in sequencing techniques (Zhang et al., 2019; Luo et al., 2010), which can limit its generalizability. We have further **re-wrote** the regularization (8) & (9) to account for the standardized covariance, which is more robust and better encompasses co-expression priors across different datasets. The re-written objective for the velocity term (8) is formulated as:

$$\sum_{\tilde{\mathcal{M}} \in \mathcal{M}_{\text{cov}}} L_{\text{corr-std}}(\pi_t, \tilde{\mathcal{M}}, 1) = \left\| \frac{d}{dt} \left(\mathbb{E}_{\pi_t} [\mathbf{x}_t \mathbf{x}_t^\top] - \mathbb{E}_{\pi_t} [\mathbf{x}_t] \mathbb{E}_{\pi_t} [\mathbf{x}_t]^\top \right) \right\|_{\text{F}}^2$$

$$= \left\| \mathbb{E}_{\pi_t} [\mathbf{x}_t \mathbf{v}_t(\mathbf{x}_t)^\top + \mathbf{v}_t(\mathbf{x}_t) \mathbf{x}_t^\top + \frac{1}{2} \boldsymbol{\Sigma}_t(\mathbf{x}_t) \boldsymbol{\Sigma}_t^\top(\mathbf{x}_t)] - \mathbb{E}_{\pi_t} [\mathbf{x}_t] \mathbb{E}_{\pi_t}^\top [\mathbf{v}_t(\mathbf{x}_t)] - \mathbb{E}_{\pi_t} [\mathbf{v}_t(\mathbf{x}_t)] \mathbb{E}_{\pi_t}^\top [\mathbf{x}_t] \right\|_F^2. \quad (10)$$

Similarly for the acceleration term (9), the standardized formulation is detailed in Appdx. E.

Furthermore, the regularizer constructed with domain-specific priors operates in a space that may not correspond to that of the data (where the diffusion generative model is built in). For instance, high-dimensional single-cell sequencing data often undergoes principal component analysis (Wold et al., 1987) prior to further processing. In this scenario, when gene expressions are linearly mapped from the principal components as $\mathbf{x}_{\text{gene}} = \mathbf{W}\mathbf{x} + \mathbf{b}$, the projected (and standardized) k -th order covariance kinetics are then represented in matrix form as:

$$\sum_{\tilde{\mathcal{M}} \in \mathcal{M}_{\text{cov}}} L_{\text{corr-std-linproj}}(\pi_t, \tilde{\mathcal{M}}, k) = \left\| \mathbf{W} \frac{d^k}{dt^k} \left(\mathbb{E}_{\pi_t} [\mathbf{x}_t \mathbf{x}_t^\top] - \mathbb{E}_{\pi_t} [\mathbf{x}_t] \mathbb{E}_{\pi_t}^\top [\mathbf{x}_t] \right) \mathbf{W}^\top \right\|_F^2. \quad (11)$$

The derivation of the more complicated, non-linear projected space is detailed in Appdx. G.

3.3.2 COVARIANCE POTENTIAL

Instantiation 3: Aligning covariance with observed bivariate interactions (“prior position”). There exists abundant observed evidence of co-expression relations among genes, sourced from numerous experiments which represent these interactions in a statistical context (Mering et al., 2003; Oughtred et al., 2019). We hope to leverage such prior knowledge in the generative modeling of cells. Specifically, denoting the observed co-expression as $\mathbf{Y} \in [0, 1]^{d \times d}$ where $Y_{[i,j]}$ is the confidence score of genes i and j being co-expressing, we construct the principled regularizer termed *covariance potential*, which borrows the idea of enforcing alignment with the “correct position” of the population states as:

$$\sum_{\tilde{\mathcal{M}} \in \mathcal{M}_{\text{cov}}} L_{\text{corr}}(\pi_t, \tilde{\mathcal{M}}, 0) = U \left(\mathbb{E}_{\pi_t} [\mathbf{x}_t \mathbf{x}_t^\top], \mathbf{Y} \right), \quad (12)$$

where $U(\cdot)$ is the designated potential function detailed in Appdx. F, and the notation $L_{\text{corr}}(\cdot)$ is reused here, as it was previously undefined for $k = 0$.

3.4 NUMERICAL SOLUTIONS TO CLSB

Approximation via unconstrained optimization. The exact solution to CLSB (6) remains challenging despite that we provide a tractable objective in Sec. 3.3, due to its non-convex objective and constraints w.r.t. network parameters. Thus, we propose a practical, approximate solution via grappling with an unconstrained optimization problem as:

$$\min_{\theta} \frac{1}{(s-1)} \sum_{i=1}^{s-1} \left(L_{\text{dist}}(\pi_{t_i+1}, \hat{p}_{t_i+1}) + \alpha_{\text{ind}} \frac{1}{d} \sum_{j=1}^d \int_{t_i}^{t_{i+1}} L_{\text{ind}}(\pi_t, j, 1) dt \right. \\ \left. + \sum_{k=0}^2 \alpha_{\text{corr},k} \frac{1}{|\mathcal{M}_{\text{cov}}|} \sum_{\tilde{\mathcal{M}} \in \mathcal{M}_{\text{cov}}} \int_{t_i}^{t_{i+1}} L_{\text{corr}}(\pi_t, \tilde{\mathcal{M}}, k) dt \right), \quad (13)$$

where $L_{\text{dist}}(\cdot)$ is the distribution discrepancy measure, and $\alpha_{\text{ind}}, \alpha_{\text{corr},0}, \alpha_{\text{corr},1}, \alpha_{\text{corr},2}$ are the weights for different regularization objectives, which are treated as hyperparameters with tuning details described in Appdx. I. Here we also adopt the individual regularizer $L_{\text{ind}}(\cdot)$ and adjust its weight α_{ind} for a more general framework encompassing Opt. (4) & (6), which is solved via gradient descent. The parametrization of neural SDEs ($\mathbf{v}_t(\cdot; \theta)$ and $\boldsymbol{\Sigma}_t(\cdot; \theta)$) is described in Appdx. H.

Extension to conditional generative modeling. We further extend CLSB into the conditional generation scenario, where we are tasked to model $(p_t(\cdot | \mathbf{c}))_{t \in [0,1]}$. The application encompasses modeling cellular systems in response to perturbations \mathbf{c} such as drug treatments or genetic mutations (Srivatsan et al., 2020; Dong et al., 2023). Such extension can be achieved by re-engineering the neural SDEs $\mathbf{v}_t(\cdot; \theta), \boldsymbol{\Sigma}_t(\cdot; \theta)$ to input additional featured conditions, which is re-written as $\mathbf{v}_t(\cdot, \mathbf{c}; \theta), \boldsymbol{\Sigma}_t(\cdot, \mathbf{c}; \theta)$, without altering the rest of the framework. We detail the neural network parametrization in Appdx. H.

4 EXPERIMENTS

We evaluate the proposed CLSB (13) in two real-world applications of modeling cellular systems in the unconditional (Sec. 4.1) and conditional generation scenarios (Sec. 4.2).

4.1 UNCONDITIONAL GENERATION: DEVELOPMENTAL MODELING OF EMBRYONIC STEM CELLS

Data. Deciphering the developmental behavior of cells is the quintessential goal in the field of stem cell research (Alison et al., 2002; Zakrzewski et al., 2019). The experiment is conducted on scRNA-seq data of embryonic stem cells (Moon et al., 2019), which is collected during the developmental stages over a period of 27 days, split into five phases: t_0 (days 0-3), t_1 (days 6-9), t_2 (days 12-15), t_3 (days 18-21), and t_4 (days 24-27). Following the setting in (Tong et al., 2020; Koshizuka & Sato, 2022), gene expressions are (linearly) projected into a lower-dimensional space through principal component analysis (PCA) (Wold et al., 1987) prior to conducting the experiments, which also can be re-projected to the original space for evaluation. We also conduct experiments on an additional cell-differentiation dataset (Weinreb et al., 2020) in Appdx. I to demonstrate the effectiveness of our method.

Evaluation and compared methods. To evaluate the (biological) validity of the proposed population regularizers, we conduct model training using data from the terminal stages (t_0, t_4) without access to the intermediate (t_1, t_2, t_3), which are held out for evaluation. Following the setting in (Tong et al., 2020; Koshizuka & Sato, 2022), the model is evaluated in the scenarios where the trajectories \mathbf{x}_{t_i} are generated based on \hat{p}_{t_0} (referred as “all-step” prediction) or based on $\hat{p}_{t_{i-1}}$ for π_{t_i} (“one-step”), and the performance is quantified for the intermediate stages, based on the discrepancy in the Wasserstein distance (Villani et al., 2009; Santambrogio, 2015) between the predicted and the ground truth principal components, using the GeomLoss library (Feydy et al., 2019).

The compared baselines include random expressions sampled from a non-informative uniform distribution and simple population average across time stamps, ODE-based approaches OT-Flow (Onken et al., 2021) and TrajectoryNet (Tong et al., 2020), and SDE-based approaches DMSB (Chen et al., 2023), NeuralSDE (Li et al., 2020; Tzen & Raginsky, 2019) and NLSB (Koshizuka & Sato, 2022). The proposed CLSB falls under the category of SDE-based approaches. We adopt neural SDEs for parametrizing dynamics, with the regularization weights tuned via grid search.

Results (i). Population regularization leads to more accurate modeling of cell developmental dynamics. The results of developmental modeling of embryonic stem cells are shown in Tab. 2. Compared with the competitors, CLSB with population regularizers alone and without individual regularizers ($\alpha_{\text{ind}} = 0$) attains the lowest average rank, predicting developmental gene expressions closest in Wasserstein distance to the ground truth. The improvement is particularly evident in the most challenging stage of t_2 , which is far from both end points observed at t_0 and t_4 . This demonstrates the effectiveness of the proposed population regularizers in the heterogeneous systems of cell clusters. We also observe that in comparison to ODE-based methods, SDE-based ones perform better, echoing the inherently stochastic and diffusive nature of cell expression priors (Koshizuka & Sato, 2022). The predicted gene-expression trajectories are visualized and compared in Fig. 2 for two genes with the highest correlation (top two rows) and for all genes along the first two principal

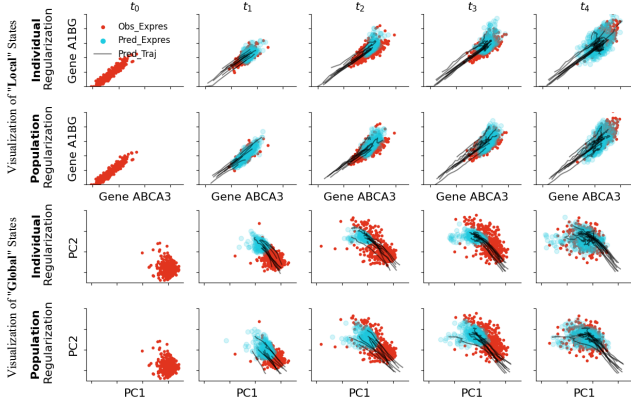


Figure 2: Visualization of the simulated gene expressions and trajectories with different methods. The trajectories are plotted for the gene pairs with the highest correlation (ABCA3 and A1BG), and along the first two PCs.

Table 2: Evaluation in the unconditional generation scenario of modeling embryonic stem-cell development. Reported are Wasserstein distances, where lower values are preferable, with means \pm standard deviations across experiments. The best and the second-best performances in each case and across cases (‘A.R.’ stands for average ranking) are highlighted in **red** and **salmon**, respectively. Methods are evaluated in the scenarios of all-step prediction on $\pi_{t_i|t_0}$ where $\pi_{t_0} = \hat{p}_{t_0}$, and one-step prediction on $\pi_{t_i|t_{i-1}}$ where $\pi_{t_{i-1}} = \hat{p}_{t_{i-1}}$, $i \in \{1, 2, 3\}$.

Methods	All-Step Prediction			One-Step Prediction			A.R.
	t_1	t_2 (Most Challenging)	t_3	t_1	t_2	t_3	
Random	1.873 \pm 0.014	2.082 \pm 0.011	1.867 \pm 0.011	1.870 \pm 0.013	2.084 \pm 0.010	1.868 \pm 0.012	10.0
SimpleAvg	1.670 \pm 0.019	1.801 \pm 0.014	1.749 \pm 0.016	1.872 \pm 0.014	2.085 \pm 0.011	1.868 \pm 0.012	9.3
OT-Flow	1.921	2.421	1.542	1.921	1.151	1.438	9.0
OT-Flow+OT	1.726	2.154	1.397	1.726	1.186	1.240	7.6
TrajectoryNet	1.774	1.888	1.076	1.774	1.178	1.315	6.8
TrajectoryNet+OT	1.134	1.336	1.008	1.134	1.151	1.132	3.6
DMSB	1.593	2.591	2.058	-	-	-	10.3
NeuralSDE	1.507 \pm 0.014	1.743 \pm 0.031	1.586 \pm 0.038	1.504 \pm 0.013	1.384 \pm 0.016	0.962 \pm 0.014	6.1
NLSB(E)	1.128 \pm 0.007	1.432 \pm 0.022	1.132 \pm 0.034	1.130 \pm 0.007	1.099 \pm 0.010	0.839 \pm 0.012	2.6
NLSB(E+D+V)	1.499 \pm 0.005	1.945 \pm 0.006	1.619 \pm 0.016	1.498 \pm 0.005	1.418 \pm 0.009	0.966 \pm 0.016	6.8
CLSB($\alpha_{\text{ind}} > 0$)	1.099 \pm 0.019	1.419 \pm 0.028	1.132 \pm 0.038	1.098 \pm 0.018	1.117 \pm 0.009	0.826 \pm 0.010	2.5
CLSB($\alpha_{\text{ind}} = 0$)	1.074 \pm 0.009	1.244 \pm 0.016	1.255 \pm 0.022	1.095 \pm 0.009	1.106 \pm 0.014	0.842 \pm 0.012	2.1

components (bottom two rows), which also qualitatively attests to the effectiveness of population regularizers. Visualizations for more gene pairs and more principal components are provided in Appdx. I. Comparison with more SOTAs (Tong et al., 2023a;b) is also shown in Tab. 12, and experiments on dataset CITE-Seq (Kim et al., 2020) at larger scale are shown in Tab. 13.

Beyond cellular systems, we also conduct more experiments on a well-controlled synthetic dataset with results shown in Tab. 15, and of other applications of opinion depolarization (Liu et al., 2022) to validate our method with results shown in Tab. 14.

(ii) Different population regularization strategies serve varied functions. We further carry out ablation studies to examine the contributions of the three population regularizers to overall performance, as detailed in Appdx. I. Interestingly, we find that they serve different functions. Specifically, restraining the ‘‘acceleration’’ of covariance ($k = 2$, instantiation 2 (9)) provides more benefit in the early stage of development (i.e. t_1), and restraining the ‘‘velocity’’ of covariance ($k = 1$, instantiation 1 (8)) does so in the later stages (i.e. t_2, t_3). This observation could indicate that in nature, co-expression relations among genes undergo larger magnitude variations in early development stages, and tend to stabilize as development progresses. The benefit of aligning with known gene-gene interactions ($k = 0$, instantiation 3 (12)) is present across all stages, albeit modestly.

4.2 CONDITIONAL GENERATION: DOSE-DEPENDENT CELLULAR RESPONSE PREDICTION TO PERTURBATIONS

Data. Examining cellular responses to chemical perturbations is one of the fundamental tasks in the drug discovery process (Dong et al., 2023; Bunne et al., 2023). The experiment utilizes the sci-Plex

Table 3: Evaluation in the conditional generation scenario of dose-dependent cellular response prediction to chemical perturbations. Numbers indicate the mean and median Wasserstein distances on all drug conditions, and the best and the second-best performances in each case and across cases (‘A.R.’ stands for average ranking) are highlighted in **red** and **salmon**, respectively.

Methods	t_1		t_2 (Most Challenging)		t_3		A.R.
	Mean	Median	Mean	Median	Mean	Median	
Random	5.236 \pm 3.349	4.895 \pm 4.080	5.215 \pm 3.416	5.037 \pm 4.311	5.247 \pm 3.346	5.011 \pm 4.108	8.0
NeuralSDE(RandInit)	2.300 \pm 1.204	2.235 \pm 1.212	2.314 \pm 1.224	2.285 \pm 1.332	2.317 \pm 1.208	2.265 \pm 1.259	7.0
VAE	1.387 \pm 0.926	1.144 \pm 0.676	1.029 \pm 0.524	0.935 \pm 0.453	0.855 \pm 0.290	0.804 \pm 0.294	4.6
NeuralODE	0.914 \pm 0.272	0.831 \pm 0.206	1.064 \pm 0.413	0.985 \pm 0.414	1.004 \pm 0.296	0.937 \pm 0.286	5.3
NeuralSDE	0.905 \pm 0.416	0.829 \pm 0.425	1.053 \pm 0.547	0.962 \pm 0.532	1.032 \pm 0.409	0.943 \pm 0.351	5.0
NLSB(E)	0.503 \pm 0.106	0.418 \pm 0.054	0.574 \pm 0.115	0.496 \pm 0.063	0.667 \pm 0.159	0.555 \pm 0.058	2.8
CLSB($\alpha_{\text{ind}} > 0$)	0.516 \pm 0.163	0.401 \pm 0.054	0.571 \pm 0.189	0.452 \pm 0.062	0.631 \pm 0.235	0.471 \pm 0.072	2.1
CLSB($\alpha_{\text{ind}} = 0$)	0.476 \pm 0.109	0.393 \pm 0.052	0.531 \pm 0.121	0.449 \pm 0.063	0.564 \pm 0.122	0.455 \pm 0.056	1.0

486 data for three cancer cell lines under different drug treatments (Srivatsan et al., 2020), where data
 487 are collected for treatment doses of 10 nM, 100 nM, 1 μ M, and 10 μ M. In this context, we consider
 488 the drug dose as pseudo-time (denoted as t_1, t_2, t_3, t_4 , respectively; whereas zero-dose control is
 489 denoted as t_0). Gene expression dynamics is conditioned on the embedding of graph-structured
 490 drug data (see more details of datasets in Appdx. H).

491 **Evaluation and compared methods.** We train our model using samples from the terminal stages
 492 (t_0, t_4), reserving samples from the intermediate stages (t_1, t_2, t_3) for evaluation. During inference,
 493 expressions are generated based on the state at t_0 . Performance is then assessed on the Wasserstein
 494 distance on PCs across all drug conditions, which is compared on the mean and median values.
 495 Evaluation on the original gene expressions is also provided in Appdx. I. The compared baselines
 496 include the random expressions, VAE (Kingma & Welling, 2013), NeuralODE (Onken et al., 2021),
 497 NeuralSDE (Li et al., 2020; Tzen & Raginsky, 2019), and NLSB (Koshizuka & Sato, 2022).

498 **Results (iv). Application of population regularization leads to more accurate prediction of**
 499 **perturbation effects.** The results of dose-dependent cellular response prediction to chemical per-
 500 turbations are shown in Tab. 3. Compared with the competitors, CLSB with population regular-
 501 ization alone ($\alpha_{\text{ind}} = 0$) attains the lowest average rank, which indicates it replicates treated gene
 502 expressions in better alignment with the ground truth, and the benefit of population regularization
 503 is presented in all the three stages. This coincides the effectiveness of the proposed population
 504 regularization. We also observe the similar phenomenon that SDE-based approaches outperform
 505 ODE-based approaches, and the classical VAE. Lastly, we split the data based on drug perturbations
 506 and showed our model’s superior predictions for new drugs in Tab. 5.

508 5 CONCLUSIONS

510 In this paper, we introduce a novel framework termed Correlational Lagrangian Schrödinger Bridge
 511 (CLSB), effectively addressing the challenges posed by restricted cross-sectional samples and the
 512 heterogeneous nature of individual particles. By shifting the focus of regularization from individual-
 513 level to population, CLSB acknowledges and leverages the inherent heterogeneity in systems to
 514 improve model generalizability. In developing CLSB, we address the technical challenges including
 515 (1) a new class of population regularizers capturing with the tractable formulation, (2) domain-
 516 informed instantiations, and (3) the integration of into data-driven generative models. Numerically,
 517 we validate the superiority of CLSB in modeling cellular systems.

518 Admittedly, there are remaining gaps that need to be filled in the future. These include, but are not
 519 limited to, the reliance on the domain-informed priors of CLSB instantiations (Sec. 3.3) and the
 520 approximability of the numerical solution (Sec. 3.4). In broader impacts, the proposed approach
 521 could be used to help develop new treatments, such as for cancer cells.

523 REFERENCES

- 524 NaumIllich Akhiezer. *The classical moment problem and some related questions in analysis*. SIAM,
 525 2020.
- 526 Malcolm R Alison, Richard Poulson, Stuart Forbes, and Nicholas A Wright. An introduction to
 527 stem cells. *The Journal of Pathology: A Journal of the Pathological Society of Great Britain and*
 528 *Ireland*, 197(4):419–423, 2002.
- 529 Alan H Barr. The einstein summation notation. *An Introduction to Physically Based Modeling*
 530 *(Course Notes 19)*, pages E, 1:57, 1991.
- 531 Charlotte Bunne, Andreas Krause, and Marco Cuturi. Supervised training of conditional monge
 532 maps. *Advances in Neural Information Processing Systems*, 35:6859–6872, 2022.
- 533 Charlotte Bunne, Stefan G Stark, Gabriele Gut, Jacobo Sarabia Del Castillo, Mitch Levesque,
 534 Kjong-Van Lehmann, Lucas Pelkmans, Andreas Krause, and Gunnar Rätsch. Learning single-
 535 cell perturbation responses using neural optimal transport. *Nature Methods*, 20(11):1759–1768,
 536 2023.

- 540 Ricky TQ Chen, Yulia Rubanova, Jesse Bettencourt, and David K Duvenaud. Neural ordinary
541 differential equations. *Advances in neural information processing systems*, 31, 2018.
- 542
- 543 Tianrong Chen, Guan-Horng Liu, Molei Tao, and Evangelos A Theodorou. Deep momentum multi-
544 marginal schrödinger bridge. *arXiv preprint arXiv:2303.01751*, 2023.
- 545 Valentin De Bortoli, James Thornton, Jeremy Heng, and Arnaud Doucet. Diffusion schrödinger
546 bridge with applications to score-based generative modeling. *Advances in Neural Information
547 Processing Systems*, 34:17695–17709, 2021.
- 548
- 549 Mingze Dong, Bao Wang, Jessica Wei, Antonio H de O. Fonseca, Curtis J Perry, Alexander Frey,
550 Ferial Ouerghi, Ellen F Foxman, Jeffrey J Ishizuka, Rahul M Dhodapkar, et al. Causal identifica-
551 tion of single-cell experimental perturbation effects with cinema-ot. *Nature Methods*, pp. 1–11,
552 2023.
- 553 Jean Feydy, Thibault Séjourné, François-Xavier Vialard, Shun-ichi Amari, Alain Trounev, and
554 Gabriel Peyré. Interpolating between optimal transport and mmd using sinkhorn divergences.
555 In *The 22nd International Conference on Artificial Intelligence and Statistics*, pp. 2681–2690,
556 2019.
- 557 Chris Finlay, Jörn-Henrik Jacobsen, Levon Nurbekyan, and Adam Oberman. How to train your
558 neural ode: the world of jacobian and kinetic regularization. In *International conference on
559 machine learning*, pp. 3154–3164. PMLR, 2020.
- 560
- 561 Arthur Frost and Ralph Pearson. Kinetics and mechanism. *The Journal of Physical Chemistry*, 65
562 (2):384–384, 1961.
- 563
- 564 Jason Gaitonde, Jon Kleinberg, and Éva Tardos. Polarization in geometric opinion dynamics. In
565 *Proceedings of the 22nd ACM Conference on Economics and Computation*, pp. 499–519, 2021.
- 566
- 567 Kevin J Gaston and John I Spicer. *Biodiversity: an introduction*. John Wiley & Sons, 2013.
- 568
- 569 Nicholas HG Holford and Lewis B Sheiner. Understanding the dose-effect relationship: clinical
570 application of pharmacokinetic-pharmacodynamic models. *Clinical pharmacokinetics*, 6(6):429–
571 453, 1981.
- 572
- 573 Steve Horvath and Jun Dong. Geometric interpretation of gene coexpression network analysis. *PLoS
574 computational biology*, 4(8):e1000117, 2008.
- 575
- 576 Gordon Keller. Embryonic stem cell differentiation: emergence of a new era in biology and
577 medicine. *Genes & development*, 19(10):1129–1155, 2005.
- 578
- 579 Hani Jieun Kim, Yingxin Lin, Thomas A Geddes, Jean Yee Hwa Yang, and Pengyi Yang. Citefuse
580 enables multi-modal analysis of cite-seq data. *Bioinformatics*, 36(14):4137–4143, 2020.
- 581
- 582 Diederik P Kingma and Max Welling. Auto-encoding variational bayes. *arXiv preprint
583 arXiv:1312.6114*, 2013.
- 584
- 585 Takeshi Koshizuka and Issei Sato. Neural lagrangian schrödinger bridge. *arXiv preprint
586 arXiv:2204.04853*, 2022.
- 587
- 588 Panqanamala Ramana Kumar and Pravin Varaiya. *Stochastic systems: Estimation, identification,
589 and adaptive control*. SIAM, 2015.
- 590
- 591 Pijush K Kundu, Ira M Cohen, and David R Dowling. *Fluid mechanics*. Academic press, 2015.
- 592
- 593 Gioele La Manno, Ruslan Soldatov, Amit Zeisel, Emelie Braun, Hannah Hochgerner, Viktor
594 Petukhov, Katja Lidschreiber, Maria E Kastriiti, Peter Lönnerberg, Alessandro Furlan, et al. Rna
595 velocity of single cells. *Nature*, 560(7719):494–498, 2018.
- 596
- 597 Xuechen Li, Ting-Kam Leonard Wong, Ricky TQ Chen, and David Duvenaud. Scalable gradients
598 for stochastic differential equations. In *International Conference on Artificial Intelligence and
599 Statistics*, pp. 3870–3882. PMLR, 2020.
- 600
- 601 EM Lifschitz and LP Pitajewski. Physical kinetics. In *Textbook of theoretical physics. 10*. 1983.

- 594 Yaron Lipman, Ricky TQ Chen, Heli Ben-Hamu, Maximilian Nickel, and Matt Le. Flow matching
595 for generative modeling. *arXiv preprint arXiv:2210.02747*, 2022.
596
- 597 Guan-Horng Liu, Tianrong Chen, Oswin So, and Evangelos Theodorou. Deep generalized
598 schrödinger bridge. *Advances in Neural Information Processing Systems*, 35:9374–9388, 2022.
- 599 Mohammad Lotfollahi, Anna Klimovskaia Susmelj, Carlo De Donno, Leon Hetzel, Yuge Ji, Igna-
600 cío L Ibarra, Sanjay R Srivatsan, Mohsen Naghipourfar, Riza M Daza, Beth Martin, et al. Predict-
601 ing cellular responses to complex perturbations in high-throughput screens. *Molecular systems*
602 *biology*, 19(6):e11517, 2023.
603
- 604 J Luo, M Schumacher, Andreas Scherer, Despoina Sanoudou, D Megherbi, T Davison, T Shi, Weida
605 Tong, Leming Shi, Huixiao Hong, et al. A comparison of batch effect removal methods for
606 enhancement of prediction performance using maqc-ii microarray gene expression data. *The*
607 *pharmacogenomics journal*, 10(4):278–291, 2010.
- 608 Evan Z Macosko, Anindita Basu, Rahul Satija, James Nemesh, Karthik Shekhar, Melissa Goldman,
609 Itay Tirosh, Allison R Bialas, Nolan Kamitaki, Emily M Martersteck, et al. Highly parallel
610 genome-wide expression profiling of individual cells using nanoliter droplets. *Cell*, 161(5):1202–
611 1214, 2015.
- 612 Emile Mathieu and Maximilian Nickel. Riemannian continuous normalizing flows. *Advances in*
613 *Neural Information Processing Systems*, 33:2503–2515, 2020.
614
- 615 Christian von Mering, Martijn Huynen, Daniel Jaeggi, Steffen Schmidt, Peer Bork, and Berend Snel.
616 String: a database of predicted functional associations between proteins. *Nucleic acids research*,
617 31(1):258–261, 2003.
- 618 Toshio Mikami. Optimal transportation problem as stochastic mechanics. *Selected Papers on Prob-*
619 *ability and Statistics, Amer. Math. Soc. Transl. Ser.*, 2(227):75–94, 2008.
620
- 621 Kevin R Moon, David van Dijk, Zheng Wang, Scott Gigante, Daniel B Burkhardt, William S Chen,
622 Kristina Yim, Antonia van den Elzen, Matthew J Hirn, Ronald R Coifman, et al. Visualizing
623 structure and transitions in high-dimensional biological data. *Nature biotechnology*, 37(12):1482–
624 1492, 2019.
- 625 Kirill Neklyudov, Rob Brekelmans, Daniel Severo, and Alireza Makhzani. Action matching: Learn-
626 ing stochastic dynamics from samples. 2023.
627
- 628 Derek Onken, Samy Wu Fung, Xingjian Li, and Lars Ruthotto. Ot-flow: Fast and accurate continu-
629 ous normalizing flows via optimal transport. In *Proceedings of the AAAI Conference on Artificial*
630 *Intelligence*, volume 35, pp. 9223–9232, 2021.
- 631 Rose Oughtred, Chris Stark, Bobby-Joe Breitkreutz, Jennifer Rust, Lorrie Boucher, Christie Chang,
632 Nadine Kolas, Lara O’Donnell, Genie Leung, Rochelle McAdam, et al. The biogrid interaction
633 database: 2019 update. *Nucleic acids research*, 47(D1):D529–D541, 2019.
634
- 635 Matteo Pariset, Ya-Ping Hsieh, Charlotte Bunne, Andreas Krause, and Valentin De Bortoli. Unbal-
636 anced diffusion schrödinger bridge. *arXiv preprint arXiv:2306.09099*, 2023.
637
- 638 Emanuel Parzen. *Stochastic processes*. SIAM, 1999.
- 639 Ashwini Patil, Kenta Nakai, and Kengo Kinoshita. Assessing the utility of gene co-expression
640 stability in combination with correlation in the analysis of protein-protein interaction networks.
641 In *BMC genomics*, volume 12, pp. 1–11. BioMed Central, 2011.
- 642 Andy Purvis and Andy Hector. Getting the measure of biodiversity. *Nature*, 405(6783):212–219,
643 2000.
644
- 645 Hannes Risken. *Fokker-planck equation*. Springer, 1996.
646
- 647 Yusuf Roohani, Kexin Huang, and Jure Leskovec. Gears: Predicting transcriptional outcomes of
novel multi-gene perturbations. *BioRxiv*, pp. 2022–07, 2022.

- 648 Filippo Santambrogio. Optimal transport for applied mathematicians. *Birkäuser, NY*, 55(58-63):94,
649 2015.
- 650
- 651 Geoffrey Schiebinger, Jian Shu, Marcin Tabaka, Brian Cleary, Vidya Subramanian, Aryeh Solomon,
652 Joshua Gould, Siyan Liu, Stacie Lin, Peter Berube, et al. Optimal-transport analysis of single-cell
653 gene expression identifies developmental trajectories in reprogramming. *Cell*, 176(4):928–943,
654 2019.
- 655 Jonas Schluter, Jonathan U Peled, Bradford P Taylor, Kate A Markey, Melody Smith, Ying Taur,
656 Rene Niehus, Anna Staffas, Anqi Dai, Emily Fontana, et al. The gut microbiota is associated with
657 immune cell dynamics in humans. *Nature*, 588(7837):303–307, 2020.
- 658
- 659 Eric Schulz, Maarten Speekenbrink, and Andreas Krause. A tutorial on gaussian process regression:
660 Modelling, exploring, and exploiting functions. *Journal of Mathematical Psychology*, 85:1–16,
661 2018.
- 662 James Alexander Shohat and Jacob David Tamarkin. *The problem of moments*, volume 1. American
663 Mathematical Society (RI), 1950.
- 664
- 665 Vignesh Ram Somnath, Matteo Pariset, Ya-Ping Hsieh, Maria Rodriguez Martinez, Andreas Krause,
666 and Charlotte Bunne. Aligned diffusion schr\”odinger bridges. *arXiv preprint arXiv:2302.11419*,
667 2023.
- 668
- 669 Yang Song, Jascha Sohl-Dickstein, Diederik P Kingma, Abhishek Kumar, Stefano Ermon, and Ben
670 Poole. Score-based generative modeling through stochastic differential equations. *arXiv preprint*
671 *arXiv:2011.13456*, 2020.
- 672 Aris Spanos. *Probability theory and statistical inference: Empirical modeling with observational*
673 *data*. Cambridge University Press, 2019.
- 674
- 675 Sriganesh Srihari and Hon Wai Leong. Temporal dynamics of protein complexes in ppi networks: a
676 case study using yeast cell cycle dynamics. In *BMC bioinformatics*, volume 13, pp. 1–9. BioMed
677 Central, 2012.
- 678 Sanjay R Srivatsan, José L McFaline-Figueroa, Vijay Ramani, Lauren Saunders, Junyue Cao,
679 Jonathan Packer, Hannah A Pliner, Dana L Jackson, Riza M Daza, Lena Christiansen, et al. Mas-
680 sively multiplex chemical transcriptomics at single-cell resolution. *Science*, 367(6473):45–51,
681 2020.
- 682
- 683 Joshua M Stuart, Eran Segal, Daphne Koller, and Stuart K Kim. A gene-coexpression network for
684 global discovery of conserved genetic modules. *science*, 302(5643):249–255, 2003.
- 685 Ella Tamir, Martin Trapp, and Arno Solin. Transport with support: Data-conditional diffusion
686 bridges. *arXiv preprint arXiv:2301.13636*, 2023.
- 687
- 688 George Temple. Gauss’s theorem in general relativity. *Proceedings of the Royal Society of London.*
689 *Series A-Mathematical and Physical Sciences*, 154(882):354–363, 1936.
- 690
- 691 Alexander Tong, Jessie Huang, Guy Wolf, David Van Dijk, and Smita Krishnaswamy. Trajectorynet:
692 A dynamic optimal transport network for modeling cellular dynamics. In *International conference*
693 *on machine learning*, pp. 9526–9536. PMLR, 2020.
- 694
- 695 Alexander Tong, Nikolay Malkin, Kilian Fatras, Lazar Atanackovic, Yanlei Zhang, Guillaume
696 Huguét, Guy Wolf, and Yoshua Bengio. Simulation-free schr\”odinger bridges via score and
697 flow matching. *arXiv preprint arXiv:2307.03672*, 2023a.
- 698
- 699 Alexander Tong, Nikolay Malkin, Guillaume Huguét, Yanlei Zhang, Jarrid Rector-Brooks, Kilian
700 Fatras, Guy Wolf, and Yoshua Bengio. Improving and generalizing flow-based generative models
701 with minibatch optimal transport. *arXiv preprint arXiv:2302.00482*, 2023b.
- Belinda Tzen and Maxim Raginsky. Neural stochastic differential equations: Deep latent gaussian
models in the diffusion limit. *arXiv preprint arXiv:1905.09883*, 2019.

702 Petar Velickovic, Guillem Cucurull, Arantxa Casanova, Adriana Romero, Pietro Lio, Yoshua Ben-
703 gio, et al. Graph attention networks. *stat*, 1050(20):10–48550, 2017.

704

705 Cédric Villani et al. *Optimal transport: old and new*, volume 338. Springer, 2009.

706

707 Pauli Virtanen, Ralf Gommers, Travis E Oliphant, Matt Haberland, Tyler Reddy, David Cournapeau,
708 Evgeni Burovski, Pearu Peterson, Warren Weckesser, Jonathan Bright, et al. Scipy 1.0: funda-
709 mental algorithms for scientific computing in python. *Nature methods*, 17(3):261–272, 2020.

710

711 Caleb Weinreb, Alejo Rodriguez-Fraticelli, Fernando D Camargo, and Allon M Klein. Lineage
712 tracing on transcriptional landscapes links state to fate during differentiation. *Science*, 367(6479):
eaaw3381, 2020.

713

714 Svante Wold, Kim Esbensen, and Paul Geladi. Principal component analysis. *Chemometrics and*
715 *intelligent laboratory systems*, 2(1-3):37–52, 1987.

716

717 Yulun Wu, Robert A Barton, Zichen Wang, Vassilis N Ioannidis, Carlo De Donno, Layne C Price,
718 Luis F Voloch, and George Karypis. Predicting cellular responses with variational causal infer-
719 ence and refined relational information. *arXiv preprint arXiv:2210.00116*, 2022.

720

721 Karren D Yang and Caroline Uhler. Scalable unbalanced optimal transport using generative adver-
722 sarial networks. *arXiv preprint arXiv:1810.11447*, 2018.

723

724 Yuning You, Tianlong Chen, Yongduo Sui, Ting Chen, Zhangyang Wang, and Yang Shen. Graph
725 contrastive learning with augmentations. *Advances in neural information processing systems*, 33:
726 5812–5823, 2020.

727

728 Yuning You, Ruida Zhou, Jiwoong Park, Haotian Xu, Chao Tian, Zhangyang Wang, and Yang Shen.
729 Latent 3d graph diffusion. In *The Twelfth International Conference on Learning Representations*,
730 2023.

731

732 Wojciech Zakrzewski, Maciej Dobrzyński, Maria Szymonowicz, and Zbigniew Rybak. Stem cells:
733 past, present, and future. *Stem cell research & therapy*, 10(1):1–22, 2019.

734

735

736

737

738

739

740

741

742

743

744

745

746

747

748

749

750

751

752

753

754

755

APPENDIX

A PROOF FOR PROPOSITION 1

Proposition 1. For revisit, correlational Lagrangian is defined as:

$$L_{\text{corr}}(\pi_t, \widetilde{\mathcal{M}}, k) = \left| \frac{d^k}{dt^k} \mathbb{E}_{\pi_t} \left[\prod_{(j,m) \in \widetilde{\mathcal{M}}} (x_{t,[j]})^m \right] \right|^2.$$

For $k = 1$, correlational Lagrangian in Opt. (6) admits the analytical expression as:

$$\begin{aligned} L_{\text{corr}}(\pi_t, \widetilde{\mathcal{M}}, 1) &= \left| \mathbb{E}_{\pi_t} \left[\nabla \left(\prod_{(j,m) \in \widetilde{\mathcal{M}}} (x_{t,[j]})^m \right) \cdot \mathbf{v}_t(\mathbf{x}_t; \theta) \right] \right. \\ &\quad \left. + \frac{1}{2} \mathbb{E}_{\pi_t} \left[(\nabla \nabla^\top \left(\prod_{(j,m) \in \widetilde{\mathcal{M}}} (x_{t,[j]})^m \right)) \cdot (\boldsymbol{\Sigma}_t(\mathbf{x}_t; \theta) \boldsymbol{\Sigma}_t^\top(\mathbf{x}_t; \theta)) \right] \right|^2, \end{aligned}$$

if for the set of functions $\mathcal{H} = \{h(\mathbf{x})\pi_t(\mathbf{x})\mathbf{v}_t(\mathbf{x}), \pi_t(\mathbf{x})\mathbf{D}(\mathbf{x})\nabla h(\mathbf{x}), \pi_t(\mathbf{x})\nabla^\top \mathbf{D}_t(\mathbf{x})h(\mathbf{x}), h(\mathbf{x})\mathbf{D}_t(\mathbf{x})\nabla \pi_t(\mathbf{x})\}$ (θ is omitted for simplicity) that $h(\mathbf{x}) = \prod_{(j,m) \in \widetilde{\mathcal{M}}} (x_{t,[j]})^m$, $\mathbf{D}_t(\mathbf{x}) = \boldsymbol{\Sigma}_t(\mathbf{x})\boldsymbol{\Sigma}_t^\top(\mathbf{x})$, it satisfies: (i) Continuity: $h' \in \mathcal{H}$ is continuously differentiable w.r.t. \mathbf{x} ; (ii) Light tail: The probability density function $\pi_t(\mathbf{x})$ is characterized by tails that are sufficiently light, such that $\oint_{S_\infty} h'(\mathbf{x}) \cdot d\mathbf{a} = 0$ for $h' \in \mathcal{H}$, where \mathbf{a} is the outward pointing unit normal on the S_∞ boundary.

Table 4: Notation settings for $k \geq 2$.

Notations	Descriptions
$\mathcal{S}_{<k>}$	Set of Operators Defining $L_{\text{corr}}(\pi_t, \widetilde{\mathcal{M}}, k)$
$\widetilde{\mathcal{S}} \in \mathcal{S}_{<k>}$	Sequence of Operators of the form $\widetilde{\mathcal{S}}' \cup \{\Upsilon'_{<i',j'>}\}$ in $\mathcal{S}_{<k>}$
$\widetilde{\mathcal{S}}'$	Sequence of Operators up to the Penultimate One in $\widetilde{\mathcal{S}}$
$\Upsilon'_{<i',j'>}$	The Last Operator in $\widetilde{\mathcal{S}}$

We here use another notation to re-express $L_{\text{corr}}(\pi_t, \widetilde{\mathcal{M}}, 1)$, in order to facilitate the following iterative derivation from $k - 1$ to k for $L_{\text{corr}}(\pi_t, \widetilde{\mathcal{M}}, k)$. Specifically, we re-express $L_{\text{corr}}(\pi_t, \widetilde{\mathcal{M}}, 1)$ in the form of:

$$\begin{aligned} L_{\text{corr}}(\pi_t, \widetilde{\mathcal{M}}, 1) &= \left| \sum_{\widetilde{\mathcal{S}} \in \{\{\nabla_{<0,0>}\}, \{(\nabla \nabla^\top)_{<0,0>}\}\}} \Gamma(\widetilde{\mathcal{S}}) \right|^2 \\ &= \left| \Gamma(\{\nabla_{<0,0>}\}) + \Gamma(\{(\nabla \nabla^\top)_{<0,0>}\}) \right|^2 \end{aligned}$$

such that we show that for all $L_{\text{corr}}(\pi_t, \widetilde{\mathcal{M}}, k)$ it can be expressed in the form of $|\sum_{\widetilde{\mathcal{S}}} \Gamma(\widetilde{\mathcal{S}})|^2$. By denoting $\mathcal{S}_{<1>} = \{\{\nabla_{<0,0>}\}, \{(\nabla \nabla^\top)_{<0,0>}\}\}$ the collection of these $\widetilde{\mathcal{S}}$ for $k = 1$, we have that for $k \geq 2$, it admits the analytical expression in an iterative manner as:

$$\begin{aligned} L_{\text{corr}}(\pi_t, \widetilde{\mathcal{M}}, k) &= \left| \sum_{\substack{\widetilde{\mathcal{S}} \in \mathcal{S}_{<k-1>} \text{ that} \\ \widetilde{\mathcal{S}} = \widetilde{\mathcal{S}}' \cup \{\Upsilon'_{<i',j'>}\}}} \Gamma(\widetilde{\mathcal{S}}' \cup \Upsilon'_{<i'+1,j'+>}) + \Gamma(\widetilde{\mathcal{S}}' \cup \Upsilon'_{<i',j'+1>}) \right. \\ &\quad \left. + \Gamma(\widetilde{\mathcal{S}} \cup \nabla_{<0,0>}) + \Gamma(\widetilde{\mathcal{S}} \cup (\nabla \nabla^\top)_{<0,0>}) \right|^2, \quad (14) \end{aligned}$$

where we denote the ordered sequence of operators $\widetilde{\mathcal{S}} = \{\dots, \Upsilon_{<i,j>}, \dots\}$ that $\Upsilon \in \{\nabla, \nabla \nabla^\top\}$, $i \in \mathbb{Z}_>$, $j \in \mathbb{Z}_>$ such that:

$$\Upsilon_{<i,j>}(\mathbf{x}) = \frac{d^i}{dt^i} \Upsilon \left(\prod_{(k,m) \in \widetilde{\mathcal{M}}} (x_{[k]})^m \right) \cdot \frac{d^j}{dt^j} \gamma(\mathbf{x}), \quad \gamma(\mathbf{x}) = \begin{cases} \mathbf{v}_t(\mathbf{x}), & \text{if } \Upsilon = \nabla \\ \boldsymbol{\Sigma}_t(\mathbf{x})\boldsymbol{\Sigma}_t^\top(\mathbf{x}), & \text{else if } \Upsilon = \nabla \nabla^\top, \end{cases}$$

and denote the function $\Gamma(\cdot)$ operating on the ordered sequence $\tilde{\mathcal{S}}$ and \circ as function composition such that:

$$\Gamma(\tilde{\mathcal{S}}) = c_{\tilde{\mathcal{S}}} \mathbb{E}_{\pi_t} [\circ_{\Upsilon_{<i,j>} \in \tilde{\mathcal{S}}} \Upsilon_{<i,j>}(\mathbf{x}_t)], \quad c_{\tilde{\mathcal{S}}} = 2^{-|\{\Upsilon_{<i,j>} : \Upsilon_{<i,j>} \in \tilde{\mathcal{S}}, \Upsilon = \nabla \nabla^\top\}|},$$

and further denote $\mathcal{S}_{<k>}$ as the set of $\tilde{\mathcal{S}}$ used to compute $L_{\text{corr}}(\pi_t, \tilde{\mathcal{M}}, k)$, e.g., $\mathcal{S}_{<1>} = \{\{\nabla_{<0,0>}\}, \{(\nabla \nabla^\top)_{<0,0>}\}\}$. With the given notations, it is noticed that $L_{\text{corr}}(\pi_t, \tilde{\mathcal{M}}, 1)$ can be rewritten in the form of Eq. (14) as $L_{\text{corr}}(\pi_t, \tilde{\mathcal{M}}, 1) = |\Gamma(\{\nabla_{<0,0>}\}) + \Gamma(\{(\nabla \nabla^\top)_{<0,0>}\})|^2$.

The conditions for if for the equality in Eq. (14) are that, for the set of functions $\mathcal{H} = \{h(\mathbf{x})\pi_t(\mathbf{x})\mathbf{v}_t(\mathbf{x}), \pi_t(\mathbf{x})\mathbf{D}(\mathbf{x})\nabla h(\mathbf{x}), \pi_t(\mathbf{x})\nabla^\top \mathbf{D}_t(\mathbf{x})h(\mathbf{x}), h(\mathbf{x})\mathbf{D}_t(\mathbf{x})\nabla \pi_t(\mathbf{x})\}$ that $h(\mathbf{x}) = \circ_{\Upsilon_{<i,j>} \in \tilde{\mathcal{S}}} \Upsilon_{<i,j>}(\mathbf{x})$, $\forall \tilde{\mathcal{S}} \in \mathcal{S}_{<k-1>}$, it satisfies: (i) Continuity. $h' \in \mathcal{H}$ is continuously differentiable w.r.t. \mathbf{x} ; (ii) Light tail. The probability density function $\pi_t(\mathbf{x})$ is characterized by tails that are sufficiently light, such that $\oint_{S_\infty} h'(\mathbf{x}) \cdot d\mathbf{a} = 0$ for $h' \in \mathcal{H}$.

Proof. Expression for $k = 1$. For simplicity, we omit θ in notations that $\mathbf{v}_t(\mathbf{x}; \theta)$, $\Sigma_t(\mathbf{x}; \theta)$ are referred as $\mathbf{v}_t(\mathbf{x})$, $\Sigma_t(\mathbf{x})$, respectively. Denoting $h : \mathbb{R}^d \rightarrow \mathbb{R}$ as the mapping satisfying the continuity and light tail conditions, for $k = 1$, we have:

$$\begin{aligned} & \frac{d}{dt} \mathbb{E}_{\pi_t} [h(\mathbf{x}_t)] \\ \stackrel{(a)}{=} & \frac{d}{dt} \int h(\mathbf{x}) \pi_t(\mathbf{x}) d\mathbf{x} = \int h(\mathbf{x}) \left(\frac{d}{dt} \pi_t(\mathbf{x}) \right) d\mathbf{x} \\ \stackrel{(b)}{=} & \int h(\mathbf{x}) \left(-\nabla \cdot (\pi_t(\mathbf{x}) \mathbf{v}_t(\mathbf{x})) + \frac{1}{2} \nabla \cdot \nabla \cdot (\pi_t(\mathbf{x}) \Sigma_t(\mathbf{x}) \Sigma_t^\top(\mathbf{x})) \right) d\mathbf{x} \\ = & \int \left(-h(\mathbf{x}) \right) \left(\nabla \cdot (\pi_t(\mathbf{x}) \mathbf{v}_t(\mathbf{x})) \right) d\mathbf{x} + \int \left(\frac{1}{2} h(\mathbf{x}) \right) \left(\nabla \cdot \nabla \cdot (\pi_t(\mathbf{x}) \Sigma_t(\mathbf{x}) \Sigma_t^\top(\mathbf{x})) \right) d\mathbf{x} \\ \stackrel{(c)}{=} & \underbrace{\int \nabla(h(\mathbf{x})) \cdot (\pi_t(\mathbf{x}) \mathbf{v}_t(\mathbf{x})) d\mathbf{x}}_{\text{Part (i)}} + \underbrace{\int -\nabla \cdot (h(\mathbf{x}) \pi_t(\mathbf{x}) \mathbf{v}_t(\mathbf{x})) d\mathbf{x}}_{\text{Part (ii)}} \\ & + \underbrace{\int -\nabla \left(\frac{1}{2} h(\mathbf{x}) \right) \cdot \left(\nabla \cdot (\pi_t(\mathbf{x}) \Sigma_t(\mathbf{x}) \Sigma_t^\top(\mathbf{x})) \right) d\mathbf{x}}_{\text{Part (iii)}} \\ & + \underbrace{\int \nabla \cdot \left(\left(\frac{1}{2} h(\mathbf{x}) \right) \left(\nabla \cdot (\pi_t(\mathbf{x}) \Sigma_t(\mathbf{x}) \Sigma_t^\top(\mathbf{x})) \right) \right) d\mathbf{x}}_{\text{Part (iv)}}, \end{aligned}$$

where (a) is attained through the standard definition of integration, (b) results from the application of the Fokker-Planck equation (2) to substitute the time derivative term with the divergence term, and (c) is achieved by applying integration by parts on the right-hand side (RHS) of Eq. (b). Next, we solve the four parts on RHS of Eq. (c). For part (i), we have:

$$\begin{aligned} & \int \nabla(h(\mathbf{x})) \cdot (\pi_t(\mathbf{x}) \mathbf{v}_t(\mathbf{x})) d\mathbf{x} \\ = & \int (\nabla h(\mathbf{x}) \cdot \mathbf{v}_t(\mathbf{x})) \pi_t(\mathbf{x}) d\mathbf{x} \\ = & \mathbb{E}_{\pi_t} [\nabla h(\mathbf{x}) \cdot \mathbf{v}_t(\mathbf{x})]. \end{aligned}$$

For part (ii), we have:

$$\begin{aligned} & \int -\nabla \cdot (h(\mathbf{x}) \pi_t(\mathbf{x}) \mathbf{v}_t(\mathbf{x})) d\mathbf{x} \\ \stackrel{(a)}{=} & - \oint_{S_\infty} (h(\mathbf{x}) \pi_t(\mathbf{x}) \mathbf{v}_t(\mathbf{x})) \cdot d\mathbf{a} \\ \stackrel{(b)}{=} & 0, \end{aligned}$$

where (a) is accomplished through the application of Gauss's theorem (Temple, 1936), that \mathbf{a} is the outward pointing unit normal at each point on the boundary at infinity S_∞ , under the satisfaction of the continuity condition, and (b) is achieved by considering the light tail condition.

For part (iii), we have:

$$\begin{aligned} & \int \nabla \left(h(\mathbf{x}) \right) \cdot \left(\nabla \cdot \left(\pi_t(\mathbf{x}) \Sigma_t(\mathbf{x}) \Sigma_t^\top(\mathbf{x}) \right) \right) d\mathbf{x} \\ \stackrel{(a)}{=} & \int \nabla \cdot \left(\pi_t(\mathbf{x}) \Sigma_t(\mathbf{x}) \Sigma_t^\top(\mathbf{x}) \nabla h(\mathbf{x}) \right) d\mathbf{x} - \int \left(\nabla \nabla^\top h(\mathbf{x}) \right) \cdot \left(\pi_t(\mathbf{x}) \Sigma_t(\mathbf{x}) \Sigma_t^\top(\mathbf{x}) \right) d\mathbf{x} \\ \stackrel{(b)}{=} & \oint_{S_\infty} \left(\pi_t(\mathbf{x}) \Sigma_t(\mathbf{x}) \Sigma_t^\top(\mathbf{x}) \nabla h(\mathbf{x}) \right) \cdot d\mathbf{a} - \mathbb{E}_{\pi_t} \left[\left(\nabla \nabla^\top h(\mathbf{x}) \right) \cdot \left(\Sigma_t(\mathbf{x}) \Sigma_t^\top(\mathbf{x}) \right) \right] \\ \stackrel{(c)}{=} & - \mathbb{E}_{\pi_t} \left[\left(\nabla \nabla^\top h(\mathbf{x}) \right) \cdot \left(\Sigma_t(\mathbf{x}) \Sigma_t^\top(\mathbf{x}) \right) \right], \end{aligned}$$

where (a) is achieved by applying integration by parts, (b) is accomplished through the application of Gauss's theorem under the satisfaction of the continuity condition, and (c) is achieved by considering the light tail condition.

For part (iv), we have:

$$\begin{aligned} & \int \nabla \cdot \left(\left(h(\mathbf{x}) \right) \left(\nabla \cdot \left(\pi_t(\mathbf{x}) \Sigma_t(\mathbf{x}) \Sigma_t^\top(\mathbf{x}) \right) \right) \right) d\mathbf{x} \\ \stackrel{(a)}{=} & \int \nabla \cdot \left(\left(h(\mathbf{x}) \right) \left(\nabla \cdot \left(\Sigma_t(\mathbf{x}) \Sigma_t^\top(\mathbf{x}) \right) \right) \pi_t(\mathbf{x}) \right) d\mathbf{x} + \int \nabla \cdot \left(\left(h(\mathbf{x}) \right) \left(\nabla \pi_t(\mathbf{x}) \cdot \left(\Sigma_t(\mathbf{x}) \Sigma_t^\top(\mathbf{x}) \right) \right) \right) d\mathbf{x} \\ \stackrel{(b)}{=} & \oint_{S_\infty} \left(\left(h(\mathbf{x}) \right) \left(\nabla \cdot \left(\Sigma_t(\mathbf{x}) \Sigma_t^\top(\mathbf{x}) \right) \right) \pi_t(\mathbf{x}) \right) \cdot d\mathbf{a} + \oint_{S_\infty} \left(\left(h(\mathbf{x}) \right) \left(\nabla \pi_t(\mathbf{x}) \cdot \left(\Sigma_t(\mathbf{x}) \Sigma_t^\top(\mathbf{x}) \right) \right) \right) \cdot d\mathbf{a} \\ \stackrel{(c)}{=} & 0, \end{aligned}$$

where (a) is achieved by applying the product rule, (b) is accomplished through the application of Gauss's theorem under the satisfaction of the continuity condition, and (c) is achieved by considering the light tail condition.

By combining them and setting $h(\mathbf{x}) = \prod_{(j,m) \in \widetilde{\mathcal{M}}} (\mathbf{x}_{[j]})^m$, we eventually have:

$$\begin{aligned} L_{\text{corr}}(\pi_t, \widetilde{\mathcal{M}}, 1) &= \left| \mathbb{E}_{\pi_t} \left[\nabla \left(\prod_{(j,m) \in \widetilde{\mathcal{M}}} (\mathbf{x}_{t,[j]})^m \right) \cdot \mathbf{v}_t(\mathbf{x}_t) \right] \right. \\ &\quad \left. + \frac{1}{2} \mathbb{E}_{\pi_t} \left[\left(\nabla \nabla^\top \left(\prod_{(j,m) \in \widetilde{\mathcal{M}}} (\mathbf{x}_{t,[j]})^m \right) \right) \cdot \left(\Sigma_t(\mathbf{x}_t) \Sigma_t^\top(\mathbf{x}_t) \right) \right] \right|^2. \end{aligned}$$

Expression for $k \geq 2$. We present a more general form of correlational Lagrangian, by denoting the ordered sequence of operators $\widetilde{\mathcal{S}} = \{\dots, \Upsilon_{<i,j>}, \dots\}$ that $\Upsilon \in \{\nabla, \nabla \nabla^\top\}$, $i \in \mathbb{Z}_>, j \in \mathbb{Z}_>$ such that

$$\Upsilon_{<i,j>}(\mathbf{x}) = \frac{d^i}{dt^i} \Upsilon \left(\prod_{(k,m) \in \widetilde{\mathcal{M}}} (x_{[k]})^m \right) \cdot \frac{d^j}{dt^j} \gamma(\mathbf{x}), \quad \gamma(\mathbf{x}) = \begin{cases} \mathbf{v}_t(\mathbf{x}), & \text{if } \Upsilon = \nabla \\ \Sigma_t(\mathbf{x}) \Sigma_t^\top(\mathbf{x}), & \text{else if } \Upsilon = \nabla \nabla^\top, \end{cases}$$

and denote the function $\Gamma(\cdot)$ operating on the ordered sequence $\widetilde{\mathcal{S}}$ such that

$$\Gamma(\widetilde{\mathcal{S}}) = c_{\widetilde{\mathcal{S}}} \mathbb{E}_{\pi_t} \left[\circ_{\Upsilon_{<i,j>} \in \widetilde{\mathcal{S}}} \Upsilon_{<i,j>}(\mathbf{x}_t) \right], \quad c_{\widetilde{\mathcal{S}}} = 2^{-|\{\Upsilon_{<i,j>} : \Upsilon_{<i,j>} \in \widetilde{\mathcal{S}}, \Upsilon = \nabla \nabla^\top\}|},$$

and then we can rewrite correlational Lagrangian for the $k = 1$ case:

$$L_{\text{corr}}(\pi_t, \widetilde{\mathcal{M}}, 1) = \left| \Gamma(\{\nabla_{<0,0>}) + \Gamma(\{(\nabla \nabla^\top)_{<0,0>}) \right|^2.$$

We further denote $\mathcal{S}_{<k>}$ as the set of $\widetilde{\mathcal{S}}$ used to compute $L_{\text{corr}}(\pi_t, \widetilde{\mathcal{M}}, k)$, e.g., $\mathcal{S}_{<1>} = \{\{\nabla_{<0,0>}, \{(\nabla \nabla^\top)_{<0,0>}\}$ according to the above formulation. Thus, for $k \geq 2$, we have:

$$L_{\text{corr}}(\pi_t, \widetilde{\mathcal{M}}, k) = \left| \sum_{\widetilde{\mathcal{S}} \in \mathcal{S}_{<k-1>}} \frac{d}{dt} \Gamma(\widetilde{\mathcal{S}}) \right|^2.$$

To calculate this general formulation, denoting $\tilde{\mathcal{S}} = \tilde{\mathcal{S}}' \cup \{\Upsilon'_{\langle i', j' \rangle}\}$, we utilize the following equation:

$$\begin{aligned}
& \frac{d}{dt} \Gamma(\tilde{\mathcal{S}}) = \frac{d}{dt} \Gamma(\tilde{\mathcal{S}}' \cup \{\Upsilon'_{\langle i', j' \rangle}\}) \\
& \stackrel{(a)}{=} c_{\tilde{\mathcal{S}}} \frac{d}{dt} \mathbb{E}_{\pi_t} [\circ_{\Upsilon_{\langle i, j \rangle} \in \tilde{\mathcal{S}}} \Upsilon_{\langle i, j \rangle}(\mathbf{x}_t)] \\
& \stackrel{(b)}{=} c_{\tilde{\mathcal{S}}} \frac{d}{dt} \int \frac{d^{i'}}{dt^{i'}} \Upsilon'(\circ_{\Upsilon_{\langle i, j \rangle} \in \tilde{\mathcal{S}}'} \Upsilon_{\langle i, j \rangle}(\mathbf{x})) \cdot \left(\frac{d^{j'}}{dt^{j'}} \gamma'(\mathbf{x}) \right) \pi_t(\mathbf{x}) d\mathbf{x} \\
& \stackrel{(c)}{=} c_{\tilde{\mathcal{S}}} \int \frac{d^{i'+1}}{dt^{i'+1}} \Upsilon'(\circ_{\Upsilon_{\langle i, j \rangle} \in \tilde{\mathcal{S}}'} \Upsilon_{\langle i, j \rangle}(\mathbf{x})) \cdot \left(\frac{d^{j'}}{dt^{j'}} \gamma'(\mathbf{x}) \right) \pi_t(\mathbf{x}) d\mathbf{x} \\
& \quad + c_{\tilde{\mathcal{S}}} \int \frac{d^{i'}}{dt^{i'}} \Upsilon'(\circ_{\Upsilon_{\langle i, j \rangle} \in \tilde{\mathcal{S}}'} \Upsilon_{\langle i, j \rangle}(\mathbf{x})) \cdot \left(\frac{d^{j'+1}}{dt^{j'+1}} \gamma'(\mathbf{x}) \right) \pi_t(\mathbf{x}) d\mathbf{x} \\
& \quad + c_{\tilde{\mathcal{S}}} \int \frac{d^{i'}}{dt^{i'}} \Upsilon'(\circ_{\Upsilon_{\langle i, j \rangle} \in \tilde{\mathcal{S}}'} \Upsilon_{\langle i, j \rangle}(\mathbf{x})) \cdot \left(\frac{d^{j'}}{dt^{j'}} \gamma'(\mathbf{x}) \right) \left(\frac{d}{dt} \pi_t(\mathbf{x}) \right) d\mathbf{x} \\
& \stackrel{(d)}{=} \Gamma(\tilde{\mathcal{S}}' \cup \{\Upsilon'_{\langle i'+1, j' \rangle}\}) + \Gamma(\tilde{\mathcal{S}}' \cup \{\Upsilon'_{\langle i', j'+1 \rangle}\}) + c_{\tilde{\mathcal{S}}} \int (\circ_{\Upsilon_{\langle i, j \rangle} \in \tilde{\mathcal{S}}} \Upsilon_{\langle i, j \rangle}(\mathbf{x})) \left(\frac{d}{dt} \pi_t(\mathbf{x}) \right) d\mathbf{x},
\end{aligned}$$

where (a, b) is established through definitions, (c) is realized by applying the product rule, and (d) is also derived from standard definitions. Denoting $h(\mathbf{x}) = \circ_{\Upsilon_{\langle i, j \rangle} \in \tilde{\mathcal{S}}} \Upsilon_{\langle i, j \rangle}(\mathbf{x})$, we have:

$$\begin{aligned}
& c_{\tilde{\mathcal{S}}} \int h(\mathbf{x}) \left(\frac{d}{dt} \pi_t(\mathbf{x}) \right) d\mathbf{x} \\
& \stackrel{(a)}{=} c_{\tilde{\mathcal{S}}} \mathbb{E}_{\pi_t} [\nabla h(\mathbf{x}) \cdot \mathbf{v}_t(\mathbf{x}_t)] + \frac{c_{\tilde{\mathcal{S}}}}{2} \mathbb{E}_{\pi_t} [(\nabla \nabla^\top (h(\mathbf{x}))) \cdot (\boldsymbol{\Sigma}_t(\mathbf{x}_t) \boldsymbol{\Sigma}_t^\top(\mathbf{x}_t))] \\
& \stackrel{(b)}{=} \Gamma(\tilde{\mathcal{S}} \cup \{\nabla_{\langle 0, 0 \rangle}\}) + \Gamma(\tilde{\mathcal{S}} \cup \{(\nabla \nabla^\top)_{\langle 0, 0 \rangle}\}),
\end{aligned}$$

where (a) follows the same derivation of correlational Lagrangian for $k = 1$, under the satisfaction of the continuity condition and light tail conditions, and (b) is established through definitions.

By combining them, we eventually have:

$$\begin{aligned}
L_{\text{corr}}(\pi_t, \tilde{\mathcal{M}}, k) = & \left| \sum_{\substack{\tilde{\mathcal{S}} \in \mathcal{S}_{\langle k-1 \rangle}, \\ \tilde{\mathcal{S}} = \tilde{\mathcal{S}}' \cup \{\Upsilon'_{\langle i', j' \rangle}\}}} \Gamma(\tilde{\mathcal{S}}' \cup \Upsilon'_{\langle i'+1, j' \rangle}) + \Gamma(\tilde{\mathcal{S}}' \cup \Upsilon'_{\langle i', j'+1 \rangle}) \right. \\
& \left. + \Gamma(\tilde{\mathcal{S}} \cup \nabla_{\langle 0, 0 \rangle}) + \Gamma(\tilde{\mathcal{S}} \cup (\nabla \nabla^\top)_{\langle 0, 0 \rangle}) \right|^2.
\end{aligned}$$

B DERIVATION OF COVARIANCE ACCELERATION

The derivation of covariance acceleration (Eq. (9)) is carried out by applying Propos. 1 (Eq. (14)) as follows:

$$\begin{aligned}
& \sum_{\tilde{\mathcal{M}} \in \mathcal{M}_{\text{cov}}} L_{\text{corr}}(\pi_t, \tilde{\mathcal{M}}, 2) = \left\| \frac{d^2}{dt^2} \mathbb{E}_{\pi_t} [\mathbf{x}_t \mathbf{x}_t^\top] \right\|_{\text{F}}^2 \\
& = \left\| \mathbb{E}_{\pi_t} \left[\underbrace{\mathbf{x}_t \left(\frac{d}{dt} \mathbf{v}_t(\mathbf{x}_t) \right)^\top + \left(\frac{d}{dt} \mathbf{v}_t(\mathbf{x}_t) \right) \mathbf{x}_t^\top + \frac{1}{2} \frac{d}{dt} (\boldsymbol{\Sigma}_t(\mathbf{x}_t) \boldsymbol{\Sigma}_t^\top(\mathbf{x}_t))}_{\Gamma(\tilde{\mathcal{S}} \cup \nabla_{\langle 0, 0 \rangle})} \right] + \underbrace{\Gamma(\tilde{\mathcal{S}}' \cup \Upsilon'_{\langle i'+1, j' \rangle})}_{\mathbf{0}} \right\|_{\text{F}}^2 \\
& \quad + \mathbb{E}_{\pi_t} \left[\underbrace{\mathbf{x}_t (\nabla \mathbf{v}_t(\mathbf{x}_t) \mathbf{v}_t(\mathbf{x}_t))^\top + (\nabla \mathbf{v}_t(\mathbf{x}_t) \mathbf{v}_t(\mathbf{x}_t)) \mathbf{x}_t^\top}_{\Gamma(\tilde{\mathcal{S}} \cup \nabla_{\langle 0, 0 \rangle})} \right] \\
& \quad + 2 \mathbf{v}_t(\mathbf{x}_t) \mathbf{v}_t(\mathbf{x}_t)^\top + \frac{1}{2} \nabla (\boldsymbol{\Sigma}_t(\mathbf{x}_t) \boldsymbol{\Sigma}_t^\top(\mathbf{x}_t))_{i_1 i_2 i_3} \mathbf{v}_t^{i_3}(\mathbf{x}_t)
\end{aligned}$$

$$\begin{aligned}
 & \Gamma(\tilde{S} \cup (\nabla \nabla^\top)_{<0,0>}) \\
 & + \mathbb{E}_{\pi_t} \left[\nabla \mathbf{v}_t(\mathbf{x}_t) \Sigma_t(\mathbf{x}_t) \Sigma_t^\top(\mathbf{x}_t) + \Sigma_t(\mathbf{x}_t) \Sigma_t^\top(\mathbf{x}_t) \nabla^\top \mathbf{v}_t(\mathbf{x}_t) \right. \\
 & + \frac{1}{2} \mathbf{x}_t (\nabla \nabla^\top (\mathbf{v}_t(\mathbf{x}_t)))_{i_1 i_2 i_3} (\Sigma_t(\mathbf{x}_t) \Sigma_t^\top(\mathbf{x}_t))^{i_2 i_3} + \frac{1}{2} (\nabla \nabla^\top (\mathbf{v}_t(\mathbf{x}_t)))_{i_1 i_2 i_3} (\Sigma_t(\mathbf{x}_t) \Sigma_t^\top(\mathbf{x}_t))^{i_2 i_3} \mathbf{x}_t^\top \\
 & \left. + \frac{1}{4} \nabla \nabla^\top (\Sigma_t(\mathbf{x}_t) \Sigma_t^\top(\mathbf{x}_t))_{i_1 i_2 i_3 i_4} (\Sigma_t(\mathbf{x}_t) \Sigma_t^\top(\mathbf{x}_t))^{i_3 i_4} \right] \Big\|_{\mathbb{F}}^2.
 \end{aligned}$$

C MORE RELATED WORKS

Modeling population dynamics with machine learning. A significant body of research has been dedicated to modeling population dynamics using data-driven approaches. This includes the development of continuous normalizing flows (Chen et al., 2018; Mathieu & Nickel, 2020), which model the dynamics through ordinary differential equations (ODEs). Furthermore, an advancement of neural ODEs, namely neural SDEs, has been introduced to capture both drift and diffusion processes using neural networks (Li et al., 2020; Tzen & Raginsky, 2019). In scenarios where ground truth trajectories are inaccessible, regularization strategies for flows have been developed. These strategies emphasize enforcing constraints on the motion of individual trajectories. Examples include the regularization of kinetic energy and its Jacobian (Tong et al., 2020; Finlay et al., 2020), as well as the inclusion of dual terms derived from the Hamilton–Jacobi–Bellman equation (Koshizuka & Sato, 2022; Onken et al., 2021), aiming to guide the model towards realistic dynamic behaviors.

In a very general sense, these methods are categorized under the optimal transport framework, characterized by varying choices of cost objectives (Somnath et al., 2023; De Bortoli et al., 2021; Bunne et al., 2023; 2022; Schiebinger et al., 2019; Neklyudov et al., 2023; Liu et al., 2022; Pariset et al., 2023; Tamir et al., 2023; You et al., 2023). It is crucial within this framework to thoughtfully construct cost functions, as they impose various priors on the dynamics data. This often leads to the imposition of homogeneous priors across all individual particles, affecting both learning accuracy and efficiency. In contrast, our work aims to model heterogeneous particle behaviors, as observed in various real-world population dynamics. For example, cell-to-cell variations in gene expression are inherent to biological systems, with changes in such variations linked to disease phenotypes and aging. Consequently, our approach enhances accuracy by employing appropriate and justifiable population-level priors to learn the dynamics of heterogeneous particles.

Developmental modeling of embryonic stem cells. The modeling of embryonic stem cell development represents a cutting-edge intersection of developmental biology, computational science, and systems biology (Alison et al., 2002; Zakrzewski et al., 2019; Weinreb et al., 2020). This field aims to unravel the complex processes governing the differentiation and proliferation of embryonic stem cells into the diverse cell types that form an organism. Given the foundational role of these processes in understanding both normal development and various diseases, developmental modeling of embryonic stem cells has garnered significant interest. At its core, developmental modeling seeks to simulate and predict the dynamic behavior of stem cells as they progress through various stages of development. This involves mapping the intricate pathways that lead to cell fate decisions, a challenge that requires sophisticated computational models and deep biological insights.

Dose-dependent cellular response prediction to chemical perturbations. The prediction of dose-dependent cellular responses to chemical perturbations is pivotal in pharmacology, toxicology, and systems biology (Dong et al., 2023; Bunne et al., 2023; Roohani et al., 2022; Lotfollahi et al., 2023). It aims to understand how cells react to varying concentrations of chemical compounds, which is crucial for drug development, safety assessment, and personalized medicine. This field combines quantitative biology, computational modeling, and high-throughput experimental techniques to map out the intricate cellular mechanisms activated or inhibited by drugs and other chemical agents at different doses. At the heart of dose-dependent cellular response prediction is the need to accurately model the complex, nonlinear interactions between chemical perturbations and cellular pathways. This involves determining the specific dose at which a chemical agent begins to have a biological effect (the threshold), the range over which the response changes (the dynamic range), and the dose causing maximal response (the ceiling).

Connection with Probability Flow Ordinary Differential Equation. Our model is able to integrate the Probability Flow Ordinary Differential Equation (Song et al., 2020) to accelerate

the sampling in scenarios where the score function can be expressed. For our parametrized SDE $dx_t = v_t(x_t)dt + \Sigma_t(x_t)d\omega_t$, the corresponding probability flow ODE sharing the same marginal probability densities is formulated as $dx_t = v_t(x_t) - \frac{1}{2}\nabla \cdot [\Sigma_t(x_t)\Sigma_t(x_t)^\top] - \frac{1}{2}\Sigma_t(x_t)\Sigma_t(x_t)^\top \nabla_x \log p_t(x_t)dt$ which requires the expression of $\nabla_x \log p_t(x_t)$ (the score function). Since $\nabla_x \log p_t(x_t)$ is in general not directly derivable, (Song et al., 2020) constructs the (known) artificial dynamics between data and white noise in a certain way such that $\nabla_x \log p_t(x_t)$ can be approximated with a neural-network parametrized score model.

Thus, in scenarios where the score function can be explicitly expressed, we are able to construct PF-ODE. An example is described as follows: p_0 is the mixture of Gaussian that $p_0(x) = \sum_{i=1}^n w_i \mathcal{N}(x; \mu_{0,i}, \sigma_{0,i}^2)$; The SDE is linear such that $v_t(x_t) = ax_t + b$, $\Sigma_t(x_t) = c$; Denoting $\mu_{t,i} = \exp(at)\mu_{0,i} + \frac{b}{a}(\exp(at) - 1)$, $\sigma_{t,i}^2 = \sigma_{0,i}^2 \exp(2at) + \frac{c^2}{2a}(\exp(2at) - 1)$; The score

function can then be expressed as $\nabla_x p_t(x_t) = \frac{\sum_{i=1}^n w_i \frac{-(x_t - \mu_{t,i})}{\sigma_{t,i}^2} \mathcal{N}(x_t; \mu_{t,i}, \sigma_{t,i}^2)}{\sum_{i=1}^n w_i \mathcal{N}(x_t; \mu_{t,i}, \sigma_{t,i}^2)}$. In the scenarios where the PF-ODE is constructed, we can speed up the sampling process via: By denoting $h_t(x_t) = v_t(x_t) - \frac{1}{2}\nabla \cdot [\Sigma_t(x_t)\Sigma_t(x_t)^\top] - \frac{1}{2}\Sigma_t(x_t)\Sigma_t(x_t)^\top \nabla_x \log p_t(x_t)$, we can then compute the exact log-likelihood via $\log p_t(x_t) = \log p_0(x_0) + \int_0^t \nabla \cdot h_s(x_s)ds$.

Connection with Flow Matching. Our model is potentially capable of integrating the flow matching objective (FM) (Lipman et al., 2022), since FM is an orthogonal objective to our proposed regularization, focusing on capturing the mismatch between generated and observed data. More specifically, FM is an alternative to the (Wasserstein) data matching loss in our framework formulated in Opt. (13). The integration can be conducted by further adding the FM loss into our optimization objective. The advantages of the FM loss are well-known: it is simple, effective in capturing distribution mismatches, and stable during training (Lipman et al., 2022). Therefore, integrating it could lead to better estimation of the terminal distribution, and faster, more stable convergence when training the diffusion model which is left to the future works.

D STABILITY OF GENETIC CO-EXPRESSION RELATIONS

Stability of genetic co-expression relations. The majority of co-expression relationships among gene pairs remain relatively stable over time, as evidenced by the first column of Fig. 3. Population regularization effectively preserves this stability, a feature that is often lost with individual-level regularization by comparing between the second and third columns of Fig. 3.

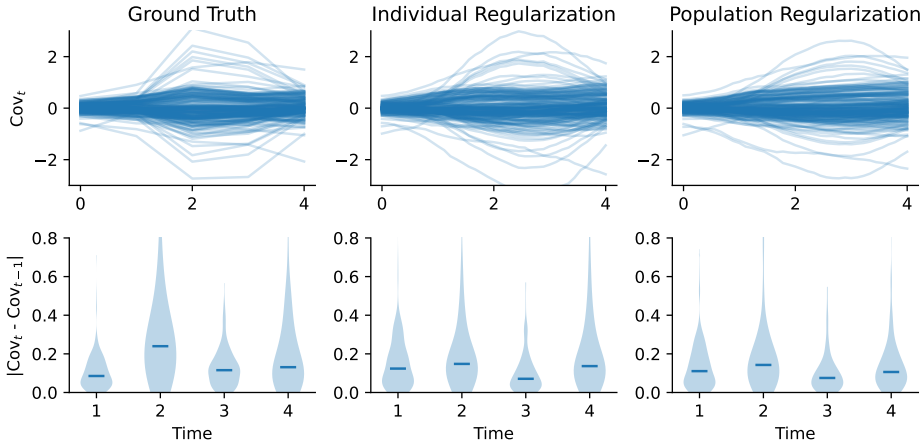


Figure 3: Visualization of temporal variations of the covariance of embryonic stem cell expression. The first row of figures presents direct plots of the covariance at time t , while the second row displays violin plots illustrating the differences between time t and $t - 1$.

E FORMULATION TO RESTRAIN ‘‘ACCELERATION’’ OF STANDARDIZED COVARIANCE

The formulation to restrain the ‘‘acceleration’’ of standardized covariance is expressed as:

$$\begin{aligned}
& \sum_{\tilde{\mathcal{M}} \in \mathcal{M}_{\text{cov}}} L_{\text{std-corr}}(\pi_t, \tilde{\mathcal{M}}, 2) = \left\| \frac{d^2}{dt^2} \left(\mathbb{E}_{\pi_t} [\mathbf{x}_t \mathbf{x}_t^\top] - \mathbb{E}_{\pi_t} [\mathbf{x}_t] \mathbb{E}_{\pi_t}^\top [\mathbf{x}_t] \right) \right\|_{\text{F}}^2 \\
& \quad \text{Matrix collection of } \Gamma(\tilde{\mathcal{S}}' \cup \Upsilon'_{\langle i', j'+1 \rangle}) \text{ terms in Eq. (14)} \\
& = \left\| \mathbb{E}_{\pi_t} \left[\mathbf{x}_t \left(\frac{d}{dt} \mathbf{v}_t(\mathbf{x}_t) \right)^\top + \left(\frac{d}{dt} \mathbf{v}_t(\mathbf{x}_t) \right) \mathbf{x}_t^\top + \frac{1}{2} \frac{d}{dt} (\boldsymbol{\Sigma}_t(\mathbf{x}_t) \boldsymbol{\Sigma}_t^\top(\mathbf{x}_t)) \right] \right. \\
& \quad - \mathbb{E}_{\pi_t} [\mathbf{x}_t] \mathbb{E}_{\pi_t}^\top \left[\frac{d}{dt} \mathbf{v}_t(\mathbf{x}_t) \right] - \mathbb{E}_{\pi_t} \left[\frac{d}{dt} \mathbf{v}_t(\mathbf{x}_t) \right] \mathbb{E}_{\pi_t}^\top [\mathbf{x}_t] \quad \left. + \underbrace{\Gamma(\tilde{\mathcal{S}}' \cup \Upsilon'_{\langle i'+1, j' \rangle})}_{\mathbf{0}} \right. \\
& \quad \left. \underbrace{\Gamma(\tilde{\mathcal{S}} \cup \nabla_{\langle 0, 0 \rangle})}_{\mathbf{0}} \right. \\
& \quad + \mathbb{E}_{\pi_t} \left[\mathbf{x}_t (\nabla(\mathbf{v}_t(\mathbf{x}_t)) \mathbf{v}_t(\mathbf{x}_t))^\top + (\nabla(\mathbf{v}_t(\mathbf{x}_t)) \mathbf{v}_t(\mathbf{x}_t)) \mathbf{x}_t^\top + 2 \mathbf{v}_t(\mathbf{x}_t) \mathbf{v}_t(\mathbf{x}_t)^\top \right. \\
& \quad \left. + \frac{1}{2} \nabla(\boldsymbol{\Sigma}_t(\mathbf{x}_t) \boldsymbol{\Sigma}_t^\top(\mathbf{x}_t))_{i_1 i_2 i_3} \mathbf{v}_t^{i_3}(\mathbf{x}_t) \right] \\
& \quad - \mathbb{E}_{\pi_t} [\mathbf{x}_t] \mathbb{E}_{\pi_t}^\top [\nabla(\mathbf{v}_t(\mathbf{x}_t)) \mathbf{v}_t(\mathbf{x}_t)] - \mathbb{E}_{\pi_t} [\nabla(\mathbf{v}_t(\mathbf{x}_t)) \mathbf{v}_t(\mathbf{x}_t)] \mathbb{E}_{\pi_t}^\top [\mathbf{x}_t] - 2 \mathbb{E}_{\pi_t} [\mathbf{v}_t(\mathbf{x}_t)] \mathbb{E}_{\pi_t}^\top [\mathbf{v}_t(\mathbf{x}_t)] \\
& \quad \left. \underbrace{\Gamma(\tilde{\mathcal{S}} \cup \nabla \nabla_{\langle 0, 0 \rangle}^\top)}_{\mathbf{0}} \right. \\
& \quad \left. + \mathbb{E}_{\pi_t} \left[\nabla(\mathbf{v}_t(\mathbf{x}_t)) \boldsymbol{\Sigma}_t(\mathbf{x}_t) \boldsymbol{\Sigma}_t^\top(\mathbf{x}_t) + \boldsymbol{\Sigma}_t(\mathbf{x}_t) \boldsymbol{\Sigma}_t^\top(\mathbf{x}_t) \nabla^\top(\mathbf{v}_t(\mathbf{x}_t)) \right. \right. \\
& \quad \left. \left. + \frac{1}{4} \nabla \nabla^\top(\boldsymbol{\Sigma}_t(\mathbf{x}_t) \boldsymbol{\Sigma}_t^\top(\mathbf{x}_t))_{i_1 i_2 i_3 i_4} (\boldsymbol{\Sigma}_t(\mathbf{x}_t) \boldsymbol{\Sigma}_t^\top(\mathbf{x}_t))^{i_3 i_4} \right. \right. \\
& \quad \left. \left. + \frac{1}{2} \mathbf{x}_t (\nabla \nabla^\top(\mathbf{v}_t(\mathbf{x}_t))_{i_1 i_2 i_3} (\boldsymbol{\Sigma}_t(\mathbf{x}_t) \boldsymbol{\Sigma}_t^\top(\mathbf{x}_t))^{i_2 i_3})^\top + \frac{1}{2} (\nabla \nabla^\top(\mathbf{v}_t(\mathbf{x}_t))_{i_1 i_2 i_3} (\boldsymbol{\Sigma}_t(\mathbf{x}_t) \boldsymbol{\Sigma}_t^\top(\mathbf{x}_t))^{i_2 i_3}) \mathbf{x}_t^\top \right] \right. \\
& \quad \left. - \frac{1}{2} \mathbb{E}_{\pi_t} [\mathbf{x}_t] \mathbb{E}_{\pi_t}^\top [\nabla \nabla^\top(\mathbf{v}_t(\mathbf{x}_t))_{i_1 i_2 i_3} (\boldsymbol{\Sigma}_t(\mathbf{x}_t) \boldsymbol{\Sigma}_t^\top(\mathbf{x}_t))^{i_2 i_3}] \right. \\
& \quad \left. - \frac{1}{2} \mathbb{E}_{\pi_t} [\nabla \nabla^\top(\mathbf{v}_t(\mathbf{x}_t))_{i_1 i_2 i_3} (\boldsymbol{\Sigma}_t(\mathbf{x}_t) \boldsymbol{\Sigma}_t^\top(\mathbf{x}_t))^{i_2 i_3}] \mathbb{E}_{\pi_t}^\top [\mathbf{x}_t] \right\|_{\text{F}}^2.
\end{aligned}$$

F FORM OF COVARIANCE POTENTIAL

Denoting $\mathbf{D} = \mathbb{E}_{\pi_t} [\mathbf{x}_t \mathbf{x}_t^\top] - \mathbb{E}_{\pi_t} [\mathbf{x}_t] \mathbb{E}_{\pi_t}^\top [\mathbf{x}_t]$, $\tilde{\mathbf{D}} \in \mathbb{R}^{d \times d}$, $\tilde{\mathbf{D}}_{[i,j]} = \begin{cases} 0, & \text{if } i \neq j \\ 1/\sqrt{\mathbf{D}_{[i,j]}}, & \text{else,} \end{cases}$, the designated form of potential covariance is expressed as:

$$\sum_{\tilde{\mathcal{M}} \in \mathcal{M}_{\text{cov}}} L_{\text{corr}}(\pi_t, \tilde{\mathcal{M}}, 0) = \left\| \tilde{\mathbf{D}}^\top \mathbf{D} \tilde{\mathbf{D}} - \mathbf{Y} \right\|_{\text{F}}^2.$$

G STANDARDIZED COVARIANCE KINETICS WITHIN A NON-LINEAR PROJECTED SPACE

We assume the diffusion generative model is built in a non-linear latent space as:

$$\mathbf{x}_t = \overleftarrow{h}(\mathbf{z}_t), \quad d\mathbf{z}_t = f(\mathbf{z}_t)dt + D(\mathbf{z}_t)d\mathbf{w}_t,$$

and then the correlation Lagrangian can be computed as:

$$\begin{aligned}
& \frac{d}{dt} \mathbb{E}[\mathbf{x}_{t,[i]} \mathbf{x}_{t,[j]}] = \frac{d}{dt} \mathbb{E}[\overleftarrow{h}_{[i]}(\mathbf{z}_t) \overleftarrow{h}_{[j]}(\mathbf{z}_t)] \\
& = \mathbb{E} \left[\nabla \{ \overleftarrow{h}_{[i]}(\mathbf{z}_t) \overleftarrow{h}_{[j]}(\mathbf{z}_t) \} \cdot f(\mathbf{z}_t) + \frac{1}{2} \nabla^2 \{ \overleftarrow{h}_{[i]}(\mathbf{z}_t) \overleftarrow{h}_{[j]}(\mathbf{z}_t) \} \cdot D^2(\mathbf{z}_t) \right] \\
& = \mathbb{E} \left[\overleftarrow{h}_{[j]}(\mathbf{z}_t) (\nabla \overleftarrow{h}_{[i]}(\mathbf{z}_t) \cdot f(\mathbf{z}_t)) + \overleftarrow{h}_{[i]}(\mathbf{z}_t) (\nabla \overleftarrow{h}_{[j]}(\mathbf{z}_t) \cdot f(\mathbf{z}_t)) \right]
\end{aligned}$$

$$+ \frac{1}{2} \left\{ \nabla \overleftarrow{h}_{[i]}(\mathbf{z}_t) \nabla \overleftarrow{h}_{[j]}^\top(\mathbf{z}_t) + \nabla \overleftarrow{h}_{[j]}(\mathbf{z}_t) \nabla \overleftarrow{h}_{[i]}^\top(\mathbf{z}_t) + \overleftarrow{h}_{[i]}(\mathbf{z}_t) \nabla^2 \overleftarrow{h}_{[j]}(\mathbf{z}_t) + \overleftarrow{h}_{[j]}(\mathbf{z}_t) \nabla^2 \overleftarrow{h}_{[i]}(\mathbf{z}_t) \right\} \cdot D^2(\mathbf{z}_t).$$

The first part of the last line can be written in the matrix form as:

$$\text{Part 1} = \mathbb{E} \left[\overleftarrow{h}(\mathbf{z}_t) (\nabla \overleftarrow{h}(\mathbf{z}_t) f(\mathbf{z}_t))^\top + (\nabla \overleftarrow{h}(\mathbf{z}_t) f(\mathbf{z}_t)) \overleftarrow{h}^\top(\mathbf{z}_t) \right].$$

The second part of the last line can be written in the matrix form as:

$$\text{Part 2} = \frac{1}{2} \mathbb{E} \left[\left\langle \left(\langle \nabla \overleftarrow{h}(\mathbf{z}_t)_{i_1 i_2}, \nabla \overleftarrow{h}(\mathbf{z}_t)_{i_3 i_4} \rangle_{i_1 i_3 i_2 i_4} + \langle \nabla \overleftarrow{h}(\mathbf{z}_t)_{i_1 i_2}, \nabla \overleftarrow{h}(\mathbf{z}_t)_{i_3 i_4} \rangle_{i_3 i_1 i_2 i_4} \right. \right. \right. \\ \left. \left. \left. + \langle \overleftarrow{h}(\mathbf{z}_t)_{i_1}, \nabla^2 \overleftarrow{h}(\mathbf{z}_t)_{i_2 i_3 i_4} \rangle_{i_1 i_2 i_3 i_4} + \langle \overleftarrow{h}(\mathbf{z}_t)_{i_1}, \nabla^2 \overleftarrow{h}(\mathbf{z}_t)_{i_2 i_3 i_4} \rangle_{i_2 i_1 i_3 i_4} \right)_{i_1 i_2 i_3 i_4}, D^2(\mathbf{z}_t)_{i_3 i_4} \right\rangle_{i_1 i_2} \right],$$

which can be simplified as follows if D is diagonal:

$$\text{Part 2} = \frac{1}{2} \mathbb{E} \left[\left\langle \left(\langle \nabla \overleftarrow{h}(\mathbf{z}_t)_{i_1 i_2}, \nabla \overleftarrow{h}(\mathbf{z}_t)_{i_3 i_2} \rangle_{i_1 i_3 i_2} + \langle \nabla \overleftarrow{h}(\mathbf{z}_t)_{i_1 i_2}, \nabla \overleftarrow{h}(\mathbf{z}_t)_{i_3 i_2} \rangle_{i_3 i_1 i_2} \right. \right. \right. \\ \left. \left. \left. + \langle \overleftarrow{h}(\mathbf{z}_t)_{i_1}, \nabla_{\text{Diag}}^2 \overleftarrow{h}(\mathbf{z}_t)_{i_2 i_3} \rangle_{i_1 i_2 i_3} + \langle \overleftarrow{h}(\mathbf{z}_t)_{i_1}, \nabla_{\text{Diag}}^2 \overleftarrow{h}(\mathbf{z}_t)_{i_2 i_3} \rangle_{i_2 i_1 i_3} \right)_{i_1 i_2 i_3}, D^2(\mathbf{z}_t)_{i_3} \right\rangle_{i_1 i_2} \right].$$

Since based on Propos. 1 we have:

$$\frac{d}{dt} \mathbb{E}[\overleftarrow{h}_{[i]}(\mathbf{z}_t)] = \mathbb{E}[\nabla \overleftarrow{h}_{[i]}(\mathbf{z}_t) \cdot f(\mathbf{z}_t) + \frac{1}{2} \nabla^2 \overleftarrow{h}_{[i]}(\mathbf{z}_t) \cdot D^2(\mathbf{z}_t)],$$

and then we can express the normalized form as:

$$\frac{d}{dt} \left(\mathbb{E}[\overleftarrow{h}(\mathbf{z}_t) \overleftarrow{h}^\top(\mathbf{z}_t)] - \mathbb{E}[\overleftarrow{h}(\mathbf{z}_t)] \mathbb{E}^\top[\overleftarrow{h}^\top(\mathbf{z}_t)] \right) \\ = \text{Part 1} + \text{Part 2} - \mathbb{E}[\overleftarrow{h}(\mathbf{z}_t)] \mathbb{E}^\top[\nabla \overleftarrow{h}(\mathbf{z}_t) f(\mathbf{z}_t)] - \mathbb{E}[\nabla \overleftarrow{h}(\mathbf{z}_t) f(\mathbf{z}_t)] \mathbb{E}^\top[\overleftarrow{h}(\mathbf{z}_t)] \\ - \frac{1}{2} \mathbb{E}[\overleftarrow{h}(\mathbf{z}_t)] \mathbb{E}^\top[\langle \nabla^2 \overleftarrow{h}(\mathbf{z}_t)_{i_1 i_2 i_3}, D^2(\mathbf{z}_t)_{i_2 i_3} \rangle_{i_1}] - \frac{1}{2} \mathbb{E}[\langle \nabla^2 \overleftarrow{h}(\mathbf{z}_t)_{i_1 i_2 i_3}, D^2(\mathbf{z}_t)_{i_2 i_3} \rangle_{i_1}] \mathbb{E}^\top[\overleftarrow{h}(\mathbf{z}_t)].$$

H NEURAL NETWORK PARAMETRIZATION OF (CONDITIONAL) NEURAL SDES

Neural network parametrization of drift $\mathbf{v}_t(\cdot; \theta)$ and diffusion $\Sigma_t(\cdot; \theta)$. We follow the architecture in (Onken et al., 2021) to parametrize the drift and diffusion functions. Specifically, given the time embedding \mathbf{z}_t for a time stamp t , we first construct a potential function $\Phi_t: \mathbb{R}^d \rightarrow \mathbb{R}$ as:

$$\Phi_t(\mathbf{x}) = \mathbf{w}^T \text{MLP}(\text{CAT}(\mathbf{x}, \mathbf{z}_t); \phi_1) + \frac{1}{2} \mathbf{x}^\top \mathbf{A}^\top \mathbf{A} \mathbf{x} + \mathbf{b}^\top \mathbf{x} + c,$$

where $\text{MLP}(\cdot; \phi_1)$ is a multi-layer perceptron, and $\text{CAT}(\cdot)$ is the concatenation function. The drift is then computed by taking the gradient as:

$$\mathbf{v}_t(\mathbf{x}; \theta) = \nabla_{\mathbf{x}} \Phi_t(\mathbf{x}).$$

For the diffusion, we simply construct it as:

$$\Sigma_t(\mathbf{x}; \theta) = \text{MLP}(\text{CAT}(\mathbf{x}, \mathbf{z}_t); \phi_2).$$

The learnable parameter collection is expressed as $\theta = \{\phi_1, \phi_2, \mathbf{w}, \mathbf{A}, \mathbf{b}, c\}$. Model predictions are generated through SDE simulation using Eq. (1) with the torchsde library (Li et al., 2020).

Neural network parametrization of conditional drift and diffusion. A small-molecule drug can be routinely represented as a graph \mathcal{G} (You et al., 2020). Thus, we leverage graph neural networks (GNNs) to embed it into vector space as $\mathbf{z}_{\mathcal{G}} = \text{GNN}(\mathcal{G}; \phi_3)$. The conditional drift and diffusion are then expressed as:

$$\mathbf{v}_t(\mathbf{x}; \theta) = \nabla_{\mathbf{x}} \left(\mathbf{w}^T \text{MLP}(\text{CAT}(\mathbf{x}, \mathbf{z}_t, \mathbf{z}_{\mathcal{G}}); \phi_1) + \frac{1}{2} \mathbf{x}^\top \mathbf{A}^\top \mathbf{A} \mathbf{x} + \mathbf{b}^\top \mathbf{x} + c \right), \\ \Sigma_t(\mathbf{x}; \theta) = \text{MLP}(\text{CAT}(\mathbf{x}, \mathbf{z}_t, \mathbf{z}_{\mathcal{G}}); \phi_2).$$

The learnable parameter collection is expressed as $\theta = \{\phi_1, \phi_2, \phi_3, \mathbf{w}, \mathbf{A}, \mathbf{b}, c\}$. We adopt the graph attention network architecture (Velickovic et al., 2017) for drug embedding.

Computational resources. Experiments are distributed on computer clusters with NVIDIA A100 GPU (40 GB memory), which in general can be finished within two days.

Additional details on the dataset of conditional generation. Dimensionality: The generative model training is conducted in 256 hidden dimensions. The hidden (latent) space is constructed by training an autoencoder on the training data, which contains the 2,000 most differentially expressed genes. Pre-processing: The pre-processing of sci-plex is standardized by adopting the code from (Wu et al., 2022). Steps include QC filtering, normalization, log1p transformation, and differentially expressed gene selection. Number of drugs: All 188 drugs contained in the dataset are used. Split: In the paper, we focus on dose-effect prediction conditional on different drug perturbations, each labeled with five dose effects (t_0 - t_4). We use the dose effects of t_0 & t_4 for training and validation, and perform testing on t_1 - t_3 as described in the main text. We also used the perturbation split to test performances on new drugs.

Regarding the significance of dose splitting, understanding the dose-effect relationship is crucial in therapeutics. Intuitively, the dose impacts drug concentration, which can lead to very different phenotypic outcomes (Holford & Sheiner, 1981). The sci-plex dataset provides treated cellular expressions under various drugs and doses. We therefore treat dose as a pseudo-time variable and construct a conditional generative model to simulate the evolution of dose effects. Similar efforts are described in (Lotfollahi et al., 2023), which are useful for guiding the clinical use of new drugs.

We also conducted an experiment using a dataset split based on drug perturbations and compared it with the SOTA CellOT (Bunne et al., 2023) in our implementation. The results, presented in Tab. 5, demonstrate the effectiveness of our method.

Table 5: Experiments on the sci-plex dataset based on drug perturbation split (predicting dose-dependent cellular response to new drugs).

Methods	VAE	CellOT	Ours
WDist ↓	8.07	1.42	1.38

I MORE RESULTS AND VISUALIZATIONS

Hyperparameter tuning. The appropriate weighting of different loss functions in the unconstrained optimization (13) for an approximated CLSB solution is important. We perform tuning for $\alpha_{\text{corr},0}$ in $\{1e-2, 1e-1, 1, 1e1, 1e2\}$, $\alpha_{\text{corr},1}$ in $\{1, 1e1, 1e2, 1e3, 1e4\}$, and $\alpha_{\text{corr},2}$ in $\{1, 1e1, 1e2, 1e3, 1e4\}$ via grid search. Validation results are shown in Tab. 6 and test results in Tab. 7. α_{ind} is tuned in $\{0, 1\}$, which does not lead to a significant impact on performance.

For the experiment in Sec. 4.1: Tab. 6 provides the validation performance for a single type of correlational regularization (out of a total of three as in Opt. (13)), and Tab. 7 showcases their corresponding test performances. The ultimate test performance in Tab. 2 is achieved by applying all three regularizations with weights tuned according to Tab. 6.

Intuition: By experimenting with the single regularization presented in Tab. 7, we aim to understand how the three types of regularizations contribute differently to the ultimate performance: Regularization on “position” provides less benefit compared to the other two; “acceleration” benefits the early stages more, and “velocity” provides more benefit in the later stages. For the experiment in Sec. 4.2: We simply adopt the hyperparameter setting from Sec. 4.1.

Evaluation of the original gene expressions in conditional generation (Sec. 4.2). We also perform evaluations on the original gene expressions beyond principal components, as shown in Tab. 8. We compute the Wasserstein distance between gene expressions and calculate both the mean and median across all drug conditions, with mean and standard deviation computed for all genes. The Wasserstein distance is computed using the SciPy library (Virtanen et al., 2020).

Table 6: Evaluation on the validation data in the unconditional generation scenario of developmental modeling of embryonic stem cells.

Methods	All-Step Prediction			One-Step Prediction		
	t_1	t_2	t_3	t_1	t_2	t_3
$\alpha_{\text{corr},0} = 0, \alpha_{\text{corr},1} = 0, \alpha_{\text{corr},2} = 0$	1.563±0.008	1.916±0.008	1.695±0.018	1.561±0.008	1.362±0.011	1.067±0.017
$\alpha_{\text{corr},0} = 1e-2, \alpha_{\text{corr},1} = 0, \alpha_{\text{corr},2} = 0$	1.532±0.008	1.886±0.012	1.670±0.016	1.533±0.007	1.356±0.011	1.051±0.018
$\alpha_{\text{corr},0} = 1e-1, \alpha_{\text{corr},1} = 0, \alpha_{\text{corr},2} = 0$	1.618±0.006	1.968±0.008	1.701±0.015	1.617±0.005	1.395±0.011	1.093±0.019
$\alpha_{\text{corr},0} = 1, \alpha_{\text{corr},1} = 0, \alpha_{\text{corr},2} = 0$	1.598±0.007	1.949±0.010	1.700±0.017	1.598±0.008	1.367±0.012	1.053±0.020
$\alpha_{\text{corr},0} = 1e1, \alpha_{\text{corr},1} = 0, \alpha_{\text{corr},2} = 0$	1.635±0.008	1.736±0.014	1.514±0.022	1.635±0.008	1.273±0.014	1.062±0.018
$\alpha_{\text{corr},0} = 1e2, \alpha_{\text{corr},1} = 0, \alpha_{\text{corr},2} = 0$	1.653±0.009	1.743±0.018	1.672±0.030	1.651±0.010	1.471±0.014	1.209±0.013
$\alpha_{\text{corr},0} = 0, \alpha_{\text{corr},1} = 1, \alpha_{\text{corr},2} = 0$	1.547±0.008	1.895±0.008	1.678±0.018	1.547±0.006	1.345±0.011	1.048±0.019
$\alpha_{\text{corr},0} = 0, \alpha_{\text{corr},1} = 1e1, \alpha_{\text{corr},2} = 0$	1.471±0.009	1.801±0.009	1.642±0.018	1.471±0.007	1.293±0.011	1.040±0.018
$\alpha_{\text{corr},0} = 0, \alpha_{\text{corr},1} = 1e2, \alpha_{\text{corr},2} = 0$	1.337±0.008	1.628±0.009	1.538±0.021	1.337±0.007	1.200±0.013	0.967±0.018
$\alpha_{\text{corr},0} = 0, \alpha_{\text{corr},1} = 1e3, \alpha_{\text{corr},2} = 0$	1.053±0.007	1.484±0.010	1.549±0.019	1.052±0.007	1.098±0.015	0.910±0.015
$\alpha_{\text{corr},0} = 0, \alpha_{\text{corr},1} = 1e4, \alpha_{\text{corr},2} = 0$	1.042±0.004	1.482±0.009	1.494±0.018	1.041±0.005	1.129±0.012	0.927±0.017
$\alpha_{\text{corr},0} = 0, \alpha_{\text{corr},1} = 0, \alpha_{\text{corr},2} = 1$	0.982±0.005	1.470±0.010	1.482±0.019	0.983±0.005	1.135±0.013	0.985±0.018
$\alpha_{\text{corr},0} = 0, \alpha_{\text{corr},1} = 0, \alpha_{\text{corr},2} = 1e1$	1.074±0.010	1.499±0.016	1.556±0.025	1.074±0.011	1.095±0.013	0.896±0.016
$\alpha_{\text{corr},0} = 0, \alpha_{\text{corr},1} = 0, \alpha_{\text{corr},2} = 1e2$	1.110±0.015	1.498±0.016	1.511±0.024	1.111±0.012	1.064±0.014	0.910±0.017
$\alpha_{\text{corr},0} = 0, \alpha_{\text{corr},1} = 0, \alpha_{\text{corr},2} = 1e3$	1.277±0.018	1.662±0.019	1.586±0.023	1.281±0.016	1.101±0.010	0.859±0.012
$\alpha_{\text{corr},0} = 0, \alpha_{\text{corr},1} = 0, \alpha_{\text{corr},2} = 1e4$	1.341±0.014	1.786±0.015	1.761±0.020	1.345±0.013	1.142±0.009	0.849±0.014

Table 7: Evaluation on the test data in the unconditional generation scenario of developmental modeling of embryonic stem cells.

Methods	All-Step Prediction			One-Step Prediction		
	t_1	t_2	t_3	t_1	t_2	t_3
$\alpha_{\text{corr},0} = 0, \alpha_{\text{corr},1} = 0, \alpha_{\text{corr},2} = 0$	1.499±0.005	1.945±0.006	1.619±0.016	1.498±0.005	1.418±0.009	0.966±0.016
$\alpha_{\text{corr},0} = 1e-2, \alpha_{\text{corr},1} = 0, \alpha_{\text{corr},2} = 0$	1.468±0.005	1.908±0.007	1.586±0.015	1.467±0.004	1.416±0.009	0.957±0.016
$\alpha_{\text{corr},0} = 0, \alpha_{\text{corr},1} = 1e3, \alpha_{\text{corr},2} = 0$	1.035±0.005	1.557±0.012	1.523±0.021	1.034±0.005	1.164±0.011	0.865±0.014
$\alpha_{\text{corr},0} = 0, \alpha_{\text{corr},1} = 0, \alpha_{\text{corr},2} = 1$	0.946±0.004	1.503±0.007	1.440±0.015	0.946±0.004	1.205±0.008	0.917±0.013

Table 8: Evaluation in the conditional generation scenario of dose-dependent cellular response prediction to chemical perturbations. Numbers ($\times 1e-3$) indicate the mean and median Wasserstein distances for all genes, where lower values are preferable.

Methods	t_1		t_2 (Most Challenging)		t_3	
	Mean	Median	Mean	Median	Mean	Median
Random	573.0±51.3	516.9±24.2	578.7±51.7	520.2±24.6	577.5±52.9	519.0±25.1
NeuralSDE(RandInit)	529.9±73.4	578.7±46.2	536.5±73.4	592.5±45.3	536.3±75.8	585.7±53.0
VAE	227.6±87.5	168.6±107.1	215.7±74.7	159.6±87.8	210.0±70.0	150.5±77.7
NeuralODE	177.7±43.2	108.3±38.7	192.3±56.1	119.8±50.0	183.5±58.4	115.5±51.4
NeuralSDE	170.1±40.8	102.0±44.8	183.0±53.2	117.3±57.1	182.3±63.4	117.8±55.0
NLSB(E)	78.6±35.1	59.8±29.3	93.1±43.1	70.0±35.8	104.0±47.9	75.9±39.6
CLSB($\alpha_{\text{ind}} > 0$)	79.3±36.4	61.0±29.6	87.3±44.8	67.0±34.6	92.0±50.0	69.4±38.1
CLSB($\alpha_{\text{ind}} = 0$)	76.9±33.7	60.9±27.4	89.1±39.9	72.2±32.5	93.3±43.2	74.8±35.4

Terminal state evaluation. Our model not only demonstrates advantages in generating the intermediate state populations between t_1 and t_3 as shown in Sec. 4, but it also excels in generating the terminal state at t_4 , as illustrated in the Tabs. 9 & 10.

Table 9: Evaluation on the terminal state t_4 for the stem-cell dataset.

Methods	OT-Flow	OT-Flow+OT	TrajectoryNet	TrajectoryNet+OT	NLSB(E)	NLSB(E+D+V)	Ours(CLSB- $\alpha > 0$)	Ours(CLSB- $\alpha = 0$)
WDist ↓	0.799	0.748	0.702	0.692	0.755	0.716	0.707	0.687

Table 10: Evaluation on the terminal state t_4 for the sci-Plex dataset.

Methods	NeuralSDE(RandInit)	VAE	NeuralODE	NeuralSDE	NLSB(E)	Ours(CLSB- $\alpha > 0$)	Ours(CLSB- $\alpha = 0$)
WDist ↓	2.26	1.03	1.04	1.07	1.28	0.80	0.70

Experiment on an additional cell-differentiation dataset. Beyond the experiment using the cell-differentiation dataset (Moon et al., 2019), we conducted additional experiments on a dataset curated from (Weinreb et al., 2020) to further validate the proposed population-level regularization. We adopted SBAlign (Somnath et al., 2023) as the base model (following the same experimental settings) and further restrained the covariance velocity (Eq. (8)) in the training objective. The results are shown in Tab. 11, demonstrating the effectiveness of our method on three out of four metrics.

Table 11: Means and standard deviations (in parentheses) of maximum-mean-discrepancy (MMD), ℓ_2 , RMSD, and cell-type classification accuracy on cellular expression simulation, following the evaluation pipeline of (Somnath et al., 2023).

Methods	MMD ↓	ℓ_2 ↓	RMSD ↓	Classification Accuracy ↑
w/o CorrLagr	1.07e-2±0.01e-2	1.24±0.02	0.21e-1±0.01e-1	56.3%±0.7%
w/ CorrLagr	1.61e-2±0.06e-2	1.07±0.04	8.93e-1±0.01e-1	57.6%±1.4%

Comparison with more SOTAs. We further compare with more baselines including (Tong et al., 2023a;b). We follow the leave-one-out setting in (Tong et al., 2023a;b) and experiment on the embryonic body dataset with results shown in Tab. 12.

Table 12: Experiments on the embryonic stem cell dataset following the leave-one-out setting in (Tong et al., 2023a)

Methods	DSBM	DSB	Reg.CFN	TrajNet	NLSB	OT-CFN	SF2M	Ours
WDist ↓	1.755	0.862	0.825	0.848	0.970	0.790	0.793	0.736

Experiment on larger and higher-dimensional dataset of CITE-Seq. We also examine the scalability of our model in the larger and higher-dimensional dataset of CITE-Seq (Kim et al., 2020). We follow the leave-one-out setting on 50 principal components as (Tong et al., 2023a), with the results shown in Tab. 13 strikingly demonstrate the distinguished scalability of our method. We believe the observed improvement is due to differences in the evaluation, where in the CITE-Seq experiment the distribution mismatch was evaluated using 50 PCs versus ≤ 10 PCs in the standard setting. Evaluating on more PCs further reveals the capability of different models in different aspects, showing how they capture the "main" distribution shifts (in the top PCs) versus how they handle "minor" distribution shifts. This interestingly demonstrates that our model effectively captures both "major" and "minor" distribution shifts during dynamic modeling.

Table 13: Experiments on the CITE-Seq dataset (high-dimensional setting) following the setting in (Tong et al., 2023a)

Methods	DSBM	I-CFM	OT-CFM	SF2M	Ours
WDist ↓	53.81	41.83	38.76	38.52	9.07

Experiment on a non-biological application of opinion depolarization. Beyond single-cell applications, we conducted experiments on the application of opinion depolarization (Gaitonde et al., 2021) to further validate the proposed population-level regularization. **Our focus is on a type of opinion dynamics that often results in strong polarization, meaning particles' opinions tend to form into distinct groups with opposite viewpoints. Take the party model as an example: particles receive random pieces of information from a predetermined distribution. They update their opinions based on these random inputs and an underlying rule: if the new information aligns with their current opinions, they are more likely to adopt it; if it contradicts, they typically reject it. This approach, known as biased assimilation, can easily lead to polarization, where the population divides into groups with strongly opposed views. For more background, we refer the readers to (Liu et al., 2022).**

The dimension of opinion depolarization is 2 following the original setting. We adopt DeepGSB (Liu et al., 2022) as the base model, maintaining the same experimental settings, with two different parametrizations for the actor-critic and critic roles. Additionally, we further restrain the covariance

velocity (Eq. (8)) in the training objective. The results are shown in Tab. 14, demonstrating the effectiveness of our method.

Table 14: Wasserstein distance between the simulation and ground-truth in the opinion depolarization experiment, following the evaluation pipeline of (Liu et al., 2022).

Methods	Actor-Critic Parametrization	Critic Parametrization
w/o CorrLagr	8.45e-2	4.09e-2
w/ CorrLagr	8.36e-2	4.02e-2

Experiment on synthetic datasets. We conduct experiments on a synthetic dataset by referencing (Tong et al., 2023a), to learn the transport from 8 Gaussian (mixture of Gaussian) to 1 Gaussian distribution. To establish an ideal setting for evaluating our proposed regularization on correlation conservativeness, we intentionally ensure that the source and target distributions have the same covariance matrix. Thus, the PDFs of the source and target distributions are formulated as follows:

- Source 8 Gaussian: $\sum_{i=1}^8 w_i \mathcal{N}(\mu_i, \Sigma_i)$ where $\sum_{i=1}^8 w_i = 1, w_i \geq 0$;
- Target 1 Gaussian: $\mathcal{N}(\mu + d, \Sigma)$ where $\mu = \sum_{i=1}^8 w_i \mu_i, \Sigma = \sum_{i=1}^8 w_i (\Sigma_i + (\mu_i - \mu)(\mu_i - \mu)^\top)$;
- Here, $\|\mathbf{d}\|$ reflects the difficulty of learning such a transport from one aspect (the larger $\|\mathbf{d}\|$, the more difficult).

Building on the SF2M base model and its training paradigm (Tong et al., 2023a), we compare the performance with and without our correlational regularization, using the Wasserstein 1 distance as the metric. The Tab. 15 results demonstrate the effectiveness of our method, especially in difficult cases.

Table 15: Wasserstein distance between the simulation and ground-truth in the synthetic experiment, following the evaluation pipeline of (Tong et al., 2023a).

$\ \mathbf{d}\ =$	50	100	200
w/o CorrLagr	1.48	1.92	3.27
w/ CorrLagr	1.39	1.63	1.77

More visualization in unconditional generation (Sec. 4.1). We provide more visualization of the simulated gene expressions (or their principal components) and trajectories as follows.

1404
1405
1406
1407
1408
1409
1410
1411
1412
1413
1414
1415
1416
1417
1418
1419
1420
1421
1422
1423
1424

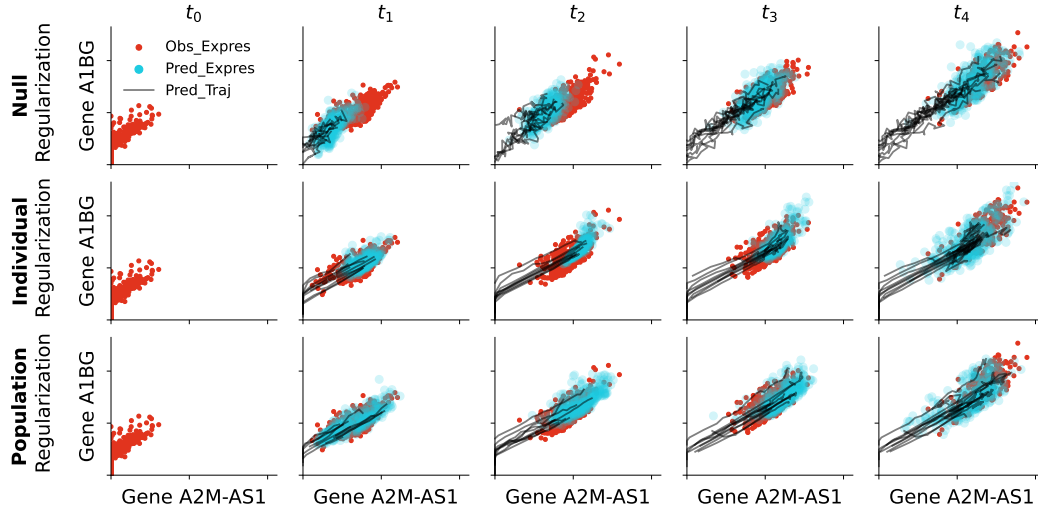


Figure 4: Visualization of local dynamics for genes A2M-AS1 and A1BG.

1425
1426
1427
1428
1429
1430
1431
1432
1433
1434
1435
1436
1437
1438
1439
1440
1441
1442
1443
1444
1445
1446
1447
1448
1449
1450
1451
1452

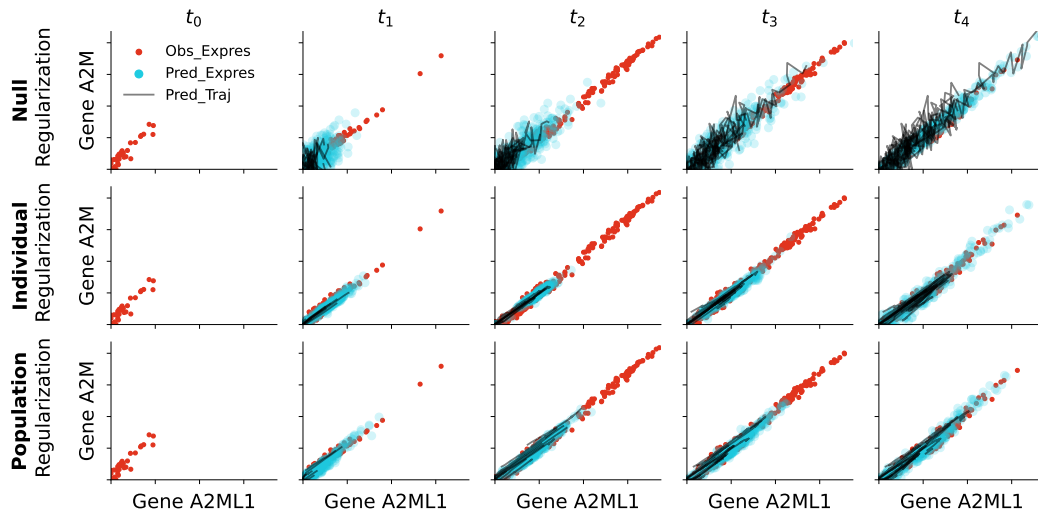


Figure 5: Visualization of local dynamics for genes A2ML1 and A2M.

1453
1454
1455
1456
1457

1458
 1459
 1460
 1461
 1462
 1463
 1464
 1465
 1466
 1467
 1468
 1469
 1470
 1471
 1472
 1473
 1474
 1475
 1476
 1477
 1478
 1479
 1480
 1481
 1482
 1483
 1484
 1485
 1486
 1487
 1488
 1489
 1490
 1491
 1492
 1493
 1494
 1495
 1496
 1497
 1498
 1499
 1500
 1501
 1502
 1503
 1504
 1505
 1506
 1507
 1508
 1509
 1510
 1511

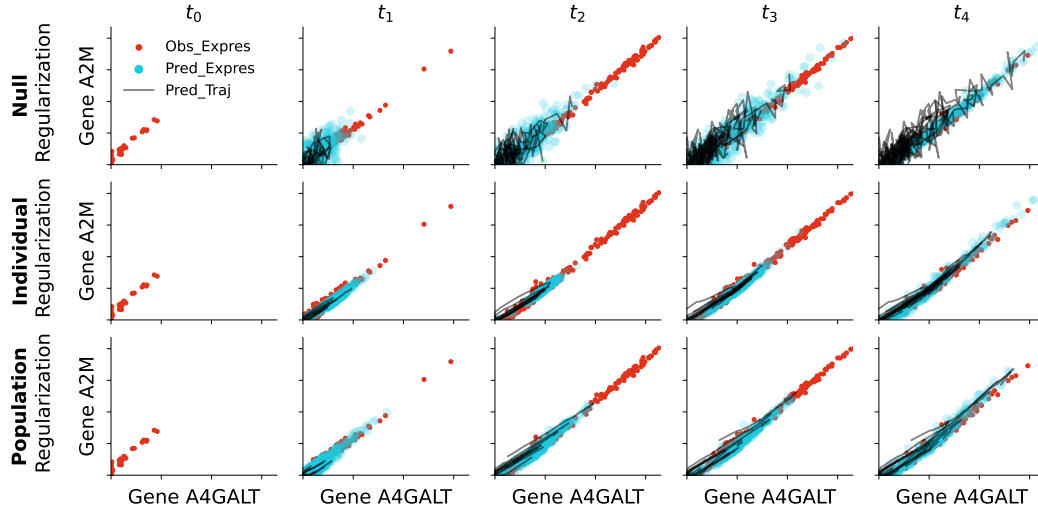


Figure 6: Visualization of local dynamics for genes A4GALT and A2M.

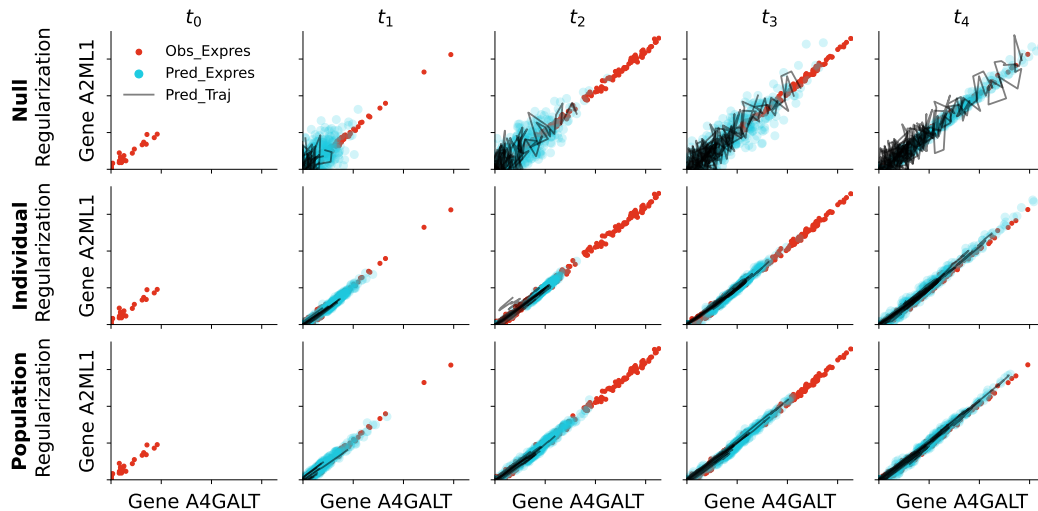


Figure 7: Visualization of local dynamics for genes A4GALT and A2ML1.

1512
 1513
 1514
 1515
 1516
 1517
 1518
 1519
 1520
 1521
 1522
 1523
 1524
 1525
 1526
 1527
 1528
 1529
 1530
 1531
 1532
 1533
 1534
 1535
 1536
 1537
 1538
 1539
 1540
 1541
 1542
 1543
 1544
 1545
 1546
 1547
 1548
 1549
 1550
 1551
 1552
 1553
 1554
 1555
 1556
 1557
 1558
 1559
 1560
 1561
 1562
 1563
 1564
 1565

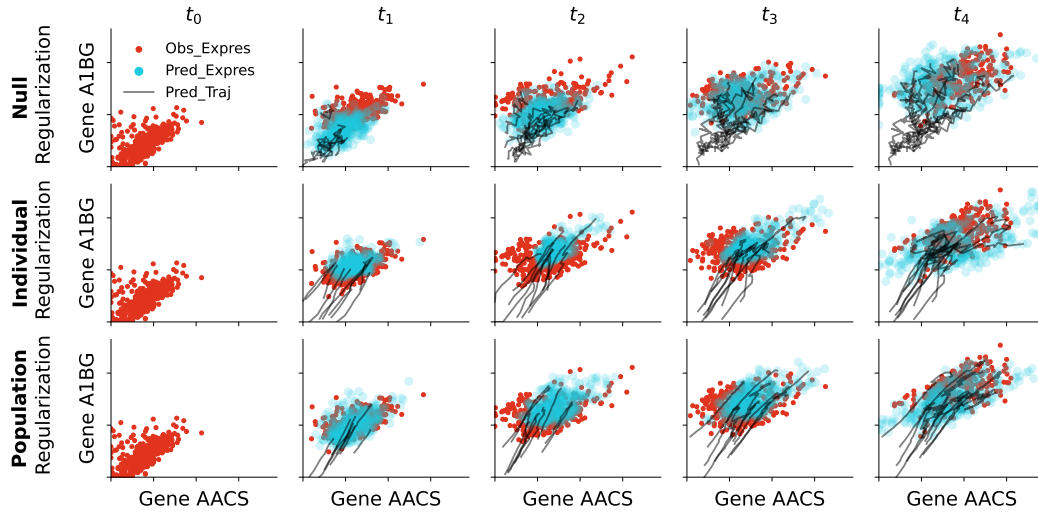


Figure 8: Visualization of local dynamics for genes AACS and A1BG.

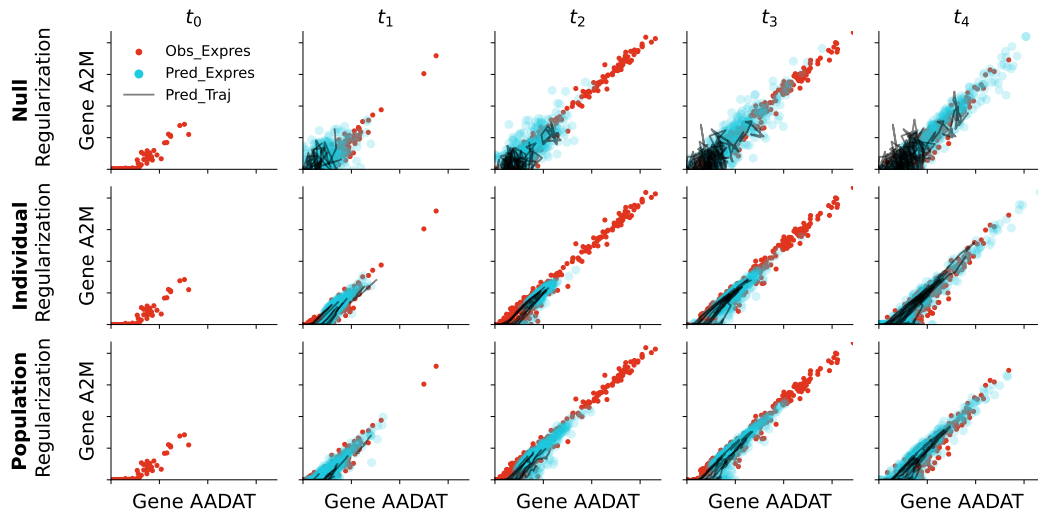


Figure 9: Visualization of local dynamics for genes AADAT and A2M.

1566
 1567
 1568
 1569
 1570
 1571
 1572
 1573
 1574
 1575
 1576
 1577
 1578
 1579
 1580
 1581
 1582
 1583
 1584
 1585
 1586
 1587
 1588
 1589
 1590
 1591
 1592
 1593
 1594
 1595
 1596
 1597
 1598
 1599
 1600
 1601
 1602
 1603
 1604
 1605
 1606
 1607
 1608
 1609
 1610
 1611
 1612
 1613
 1614
 1615
 1616
 1617
 1618
 1619

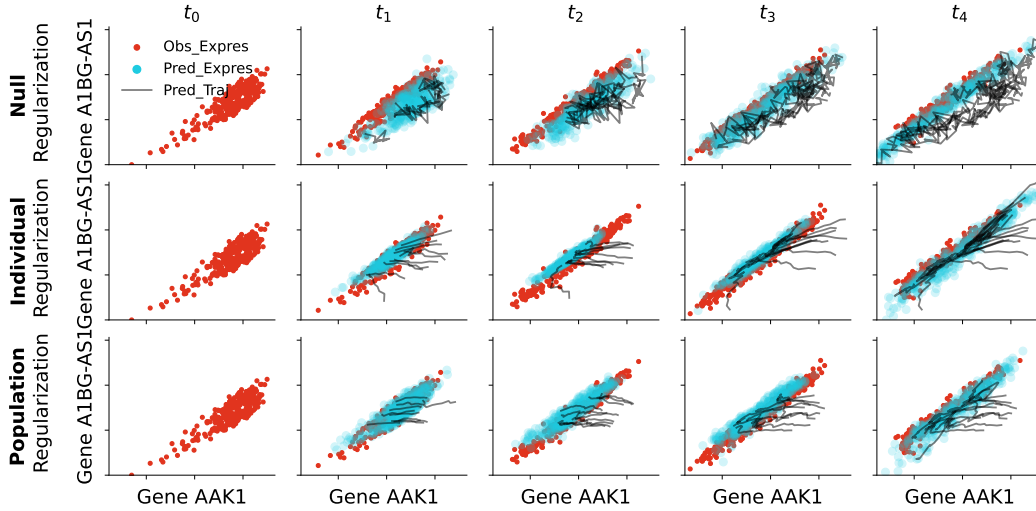


Figure 10: Visualization of local dynamics for genes AAK1 and A1BG-AS1.

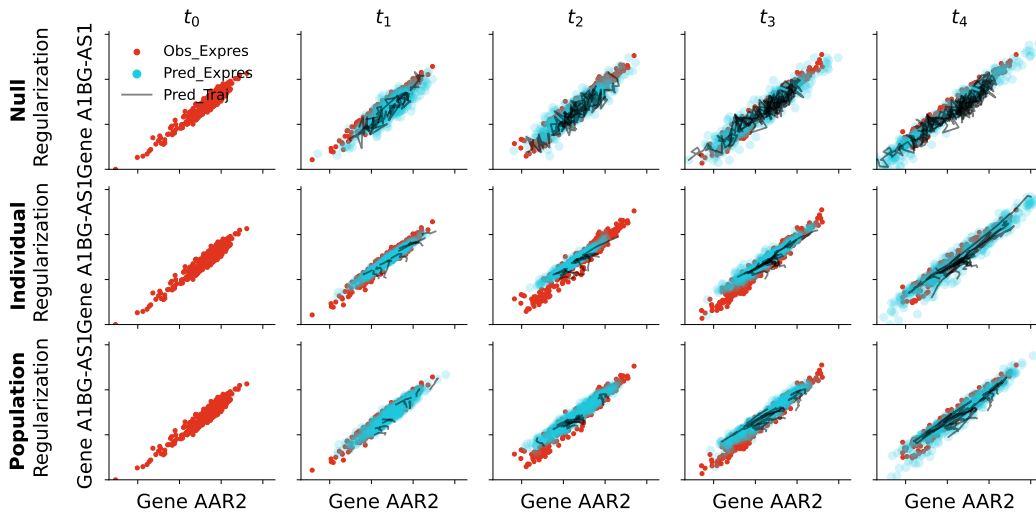


Figure 11: Visualization of local dynamics for genes AAR2 and A1BG-AS1.

1620
1621
1622
1623
1624
1625
1626
1627
1628
1629
1630
1631
1632
1633
1634
1635
1636
1637
1638
1639
1640
1641
1642
1643
1644
1645
1646
1647
1648
1649
1650
1651
1652
1653
1654
1655
1656
1657
1658
1659
1660
1661
1662
1663
1664
1665
1666
1667
1668
1669
1670
1671
1672
1673

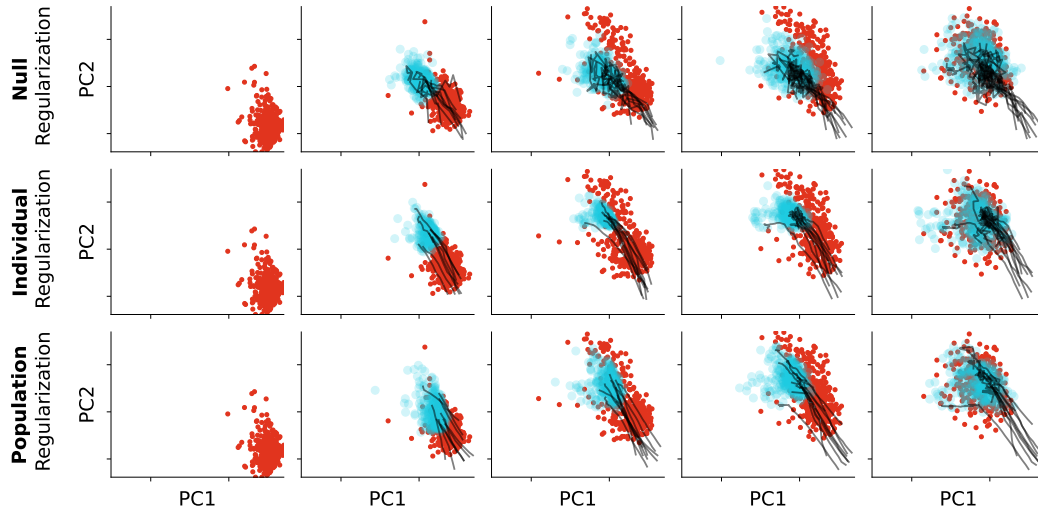


Figure 12: Visualization of global dynamics for principle components 1 and 2.

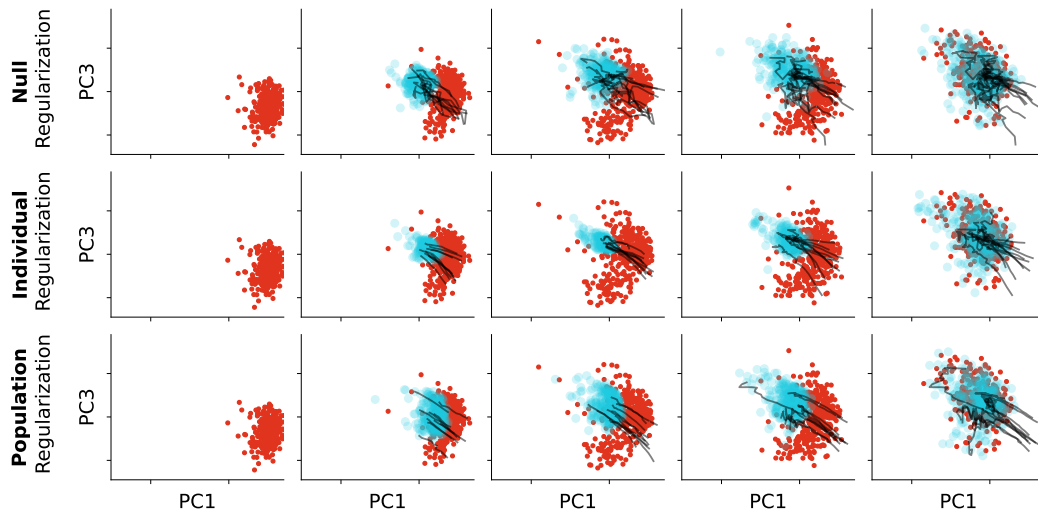


Figure 13: Visualization of global dynamics for principle components 1 and 3.

1674
1675
1676
1677
1678
1679
1680
1681
1682
1683
1684
1685
1686
1687
1688
1689
1690
1691
1692
1693
1694
1695
1696
1697
1698
1699
1700
1701
1702
1703
1704
1705
1706
1707
1708
1709
1710
1711
1712
1713
1714
1715
1716
1717
1718
1719
1720
1721
1722
1723
1724
1725
1726
1727

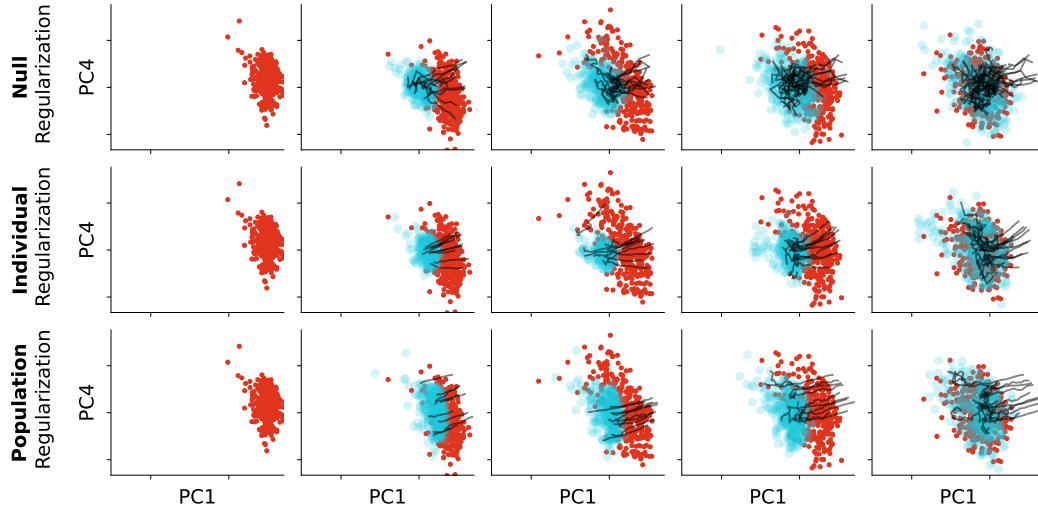


Figure 14: Visualization of global dynamics for principle components 1 and 4.

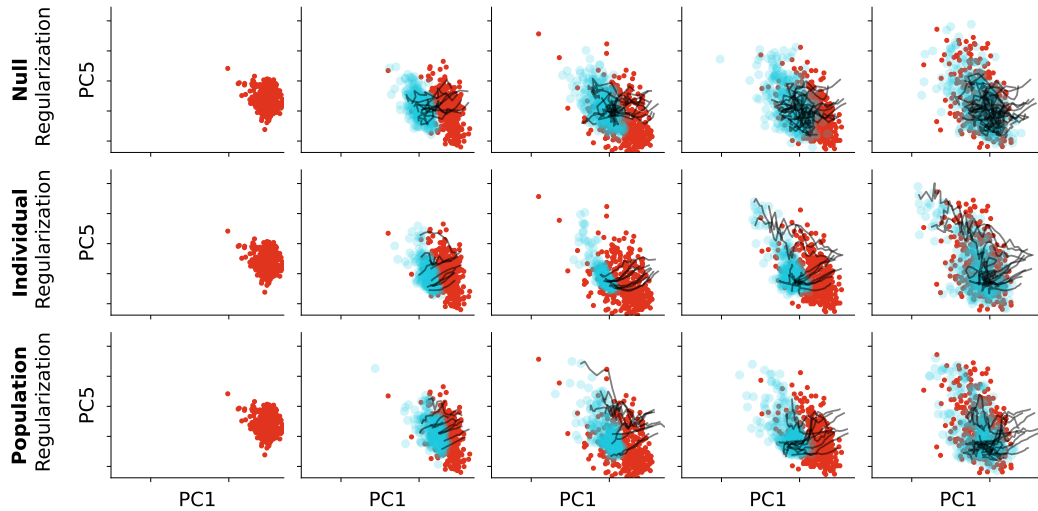


Figure 15: Visualization of global dynamics for principle components 1 and 5.

1728
1729
1730
1731
1732
1733
1734
1735
1736
1737
1738
1739
1740
1741
1742
1743
1744
1745
1746
1747
1748
1749
1750
1751
1752
1753
1754
1755
1756
1757
1758
1759
1760
1761
1762
1763
1764
1765
1766
1767
1768
1769
1770
1771
1772
1773
1774
1775
1776
1777
1778
1779
1780
1781

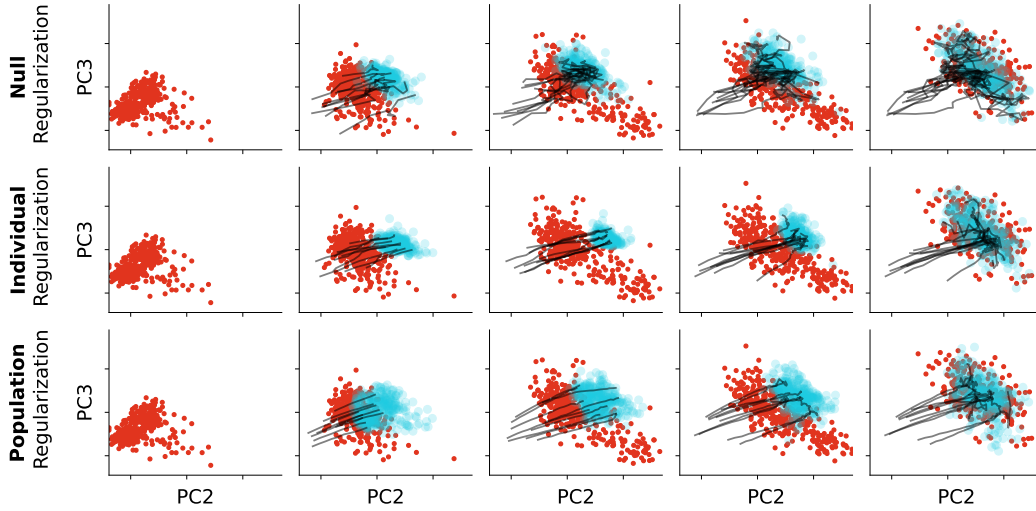


Figure 16: Visualization of global dynamics for principle components 2 and 3.

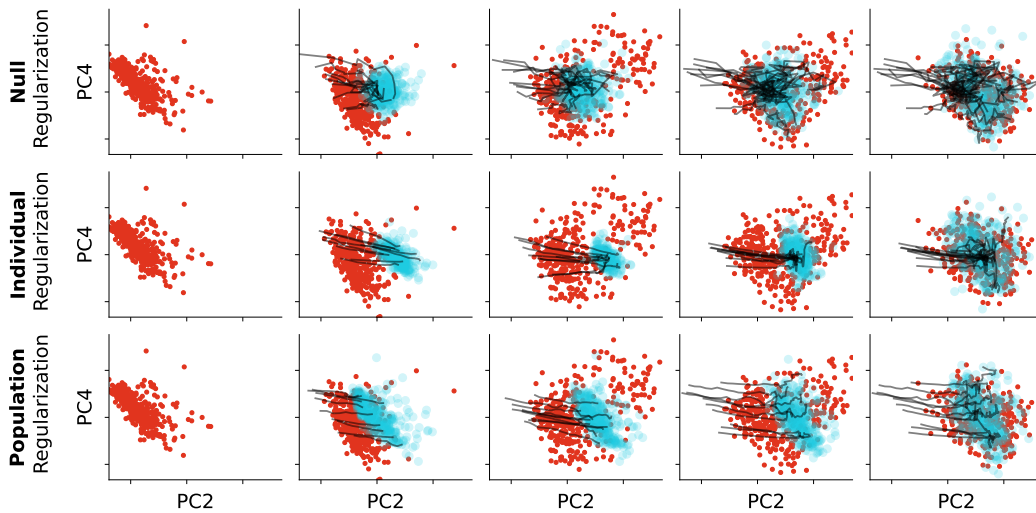


Figure 17: Visualization of global dynamics for principle components 2 and 4.

1782
1783
1784
1785
1786
1787
1788
1789
1790
1791
1792
1793
1794
1795
1796
1797
1798
1799
1800
1801
1802
1803
1804
1805
1806
1807
1808
1809
1810
1811
1812
1813
1814
1815
1816
1817
1818
1819
1820
1821
1822
1823
1824
1825
1826
1827
1828
1829
1830
1831
1832
1833
1834
1835

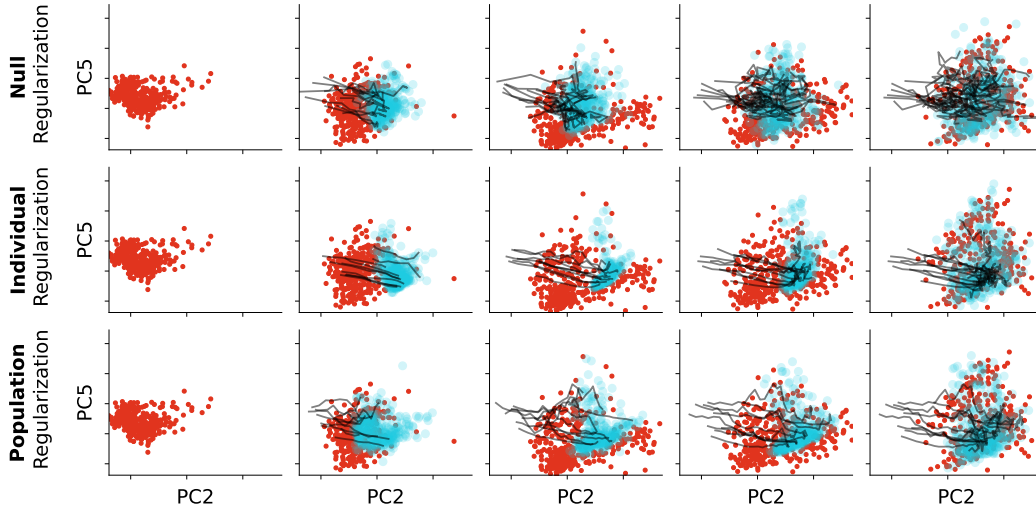


Figure 18: Visualization of global dynamics for principle components 2 and 5.

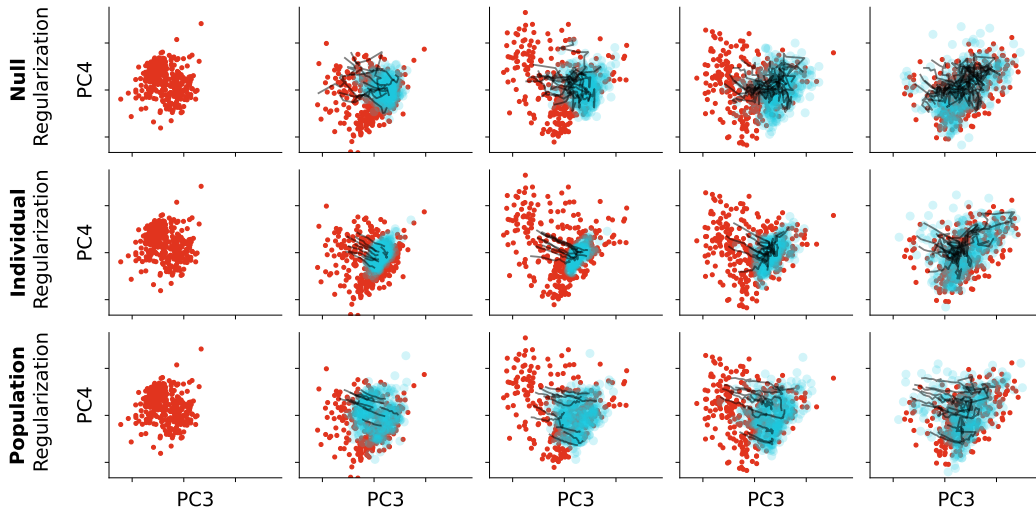


Figure 19: Visualization of global dynamics for principle components 3 and 4.

1836
1837
1838
1839
1840
1841
1842
1843
1844
1845
1846
1847
1848
1849
1850
1851
1852
1853
1854
1855
1856
1857
1858
1859
1860
1861
1862
1863
1864
1865
1866
1867
1868
1869
1870
1871
1872
1873
1874
1875
1876
1877
1878
1879
1880
1881
1882
1883
1884
1885
1886
1887
1888
1889

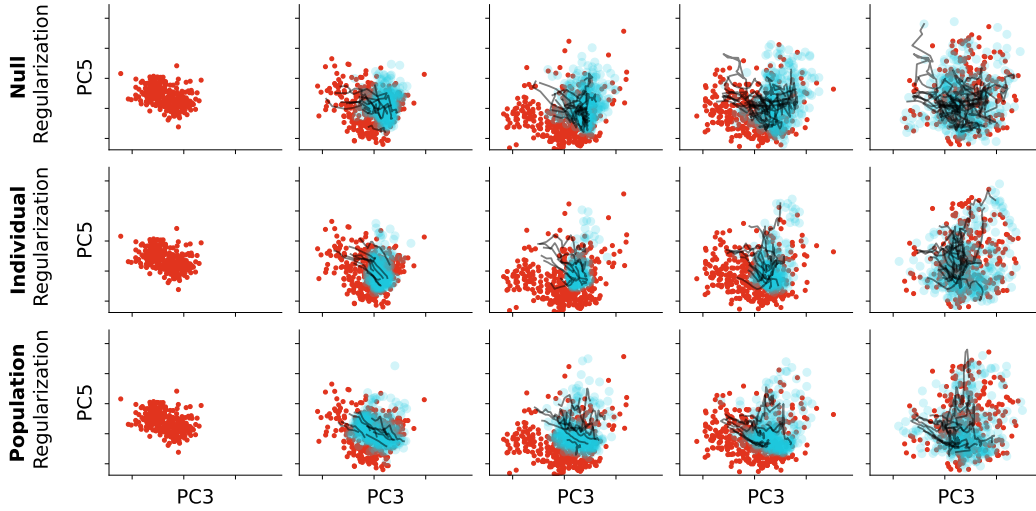


Figure 20: Visualization of global dynamics for principle components 3 and 5.

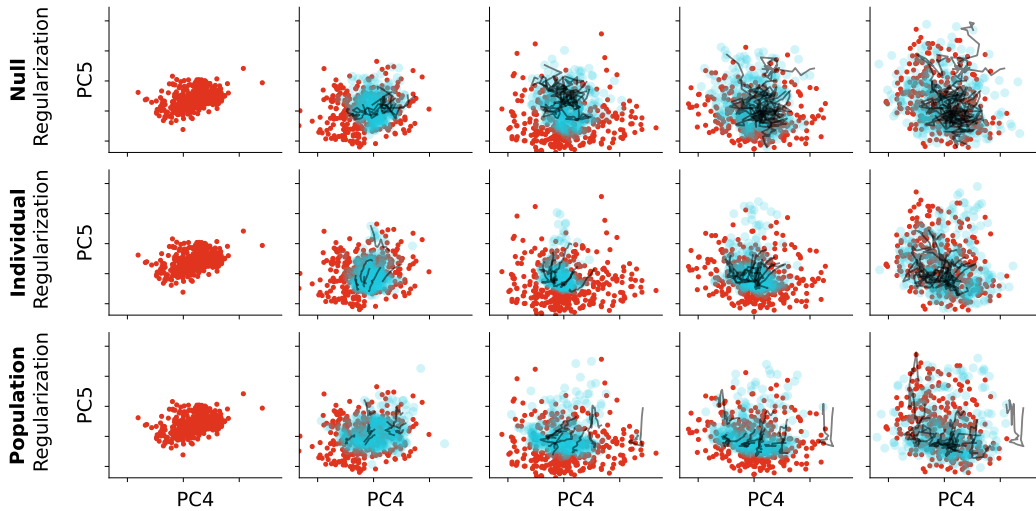


Figure 21: Visualization of global dynamics for principle components 4 and 5.

1890
1891
1892
1893
1894
1895
1896
1897
1898
1899
1900
1901
1902
1903
1904
1905
1906
1907
1908
1909
1910
1911
1912
1913
1914
1915
1916
1917
1918
1919
1920
1921
1922
1923
1924
1925
1926
1927
1928
1929
1930
1931
1932
1933
1934
1935
1936
1937
1938
1939
1940
1941
1942
1943

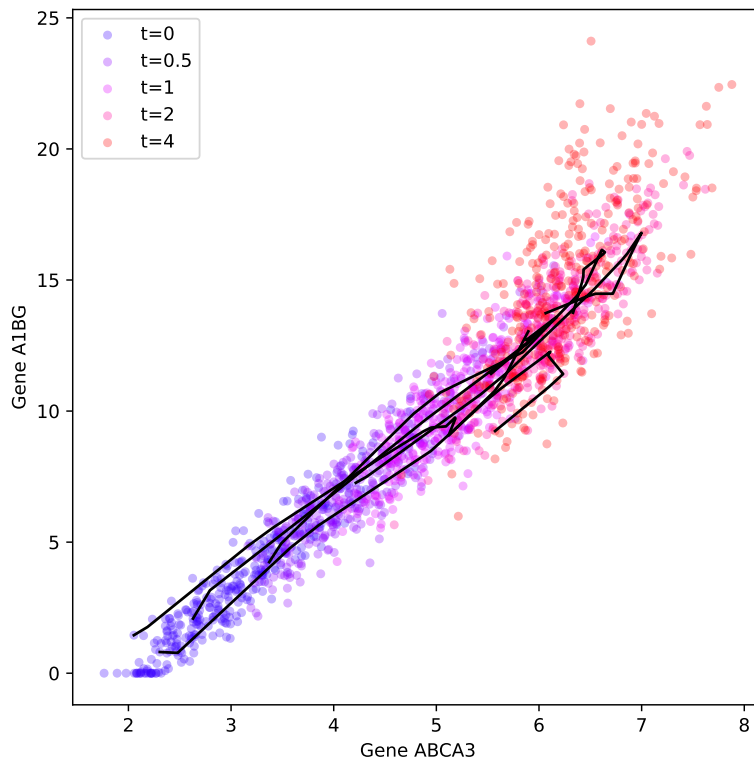


Figure 22: Aggregated visualization of generated dynamics for Fig. 2.